MŰEGYETEM 1782

MSc. Thesis

Optically detected magnetic resonance on single-walled carbon nanotubes

Julianna Palotás

Thesis advisor: Ferenc Simon
Professor
Department of Physics
Institute of Physics
BME

Budapest University of Technology and Economics

BME
2017.

Contents

A szakdolgozat kiírása

Az új anyagok optikai tulajdonságainak megértése igen fontos a potenciális optoelektronikai és fotovoltaikus alkalmazásaik szempontjából. Ezen belül is a gerjesztett, nem spin-megengedett triplett állapotok vizsgálata lényeges. Nemrégiben megfigyeltük az ún. optikailag detektált mágneses rezonancia (ODMR) jelet szén nanocsöveken. A munka során számos kérdés merült fel. Pl. a gerjesztett triplett állapotok élettartama, a triplet állapotok konverziós rátái, a legoptimálisabb szén nanocső minta előállítási módszere stb. A jelentkező feladata, hogy ebbe a munkába kapcsolódjon be, ezen nyitott kérdések megválaszolására. A közeli jövőben helyezünk üzembe egy nagyteljesítményű Q kapcsolt lézert, amivel az időfelbontott mérések is lehetővé vállnak. A munka során az időfelbontott ODMR berendezés kifejlesztése is a feladatok közé tartozik.

Önállósági nyilatkozat

Alulírott Palotás Julianna, a Budapesti Mûszaki és Gazdaságtudományi Egyetem hallgatója kijelentem, hogy ezt a szakdolgozatot meg nem engedett segédeszközök nélkül, saját magam készítettem, és csak a megadott forrásokat használtam fel. Minden olyan szövegrészt, adatot, diagramot, ábrát, amelyet azonos értelemben más forrásból átvettem, egyértelműen, a forrás megadásával megjelöltem.

Budapest, 2017. május 26.

Palotás Julianna

Köszönetnyilvánítás

Szeretném megköszönni témavezetőmnek, Prof. Simon Ferencnek segítségét, türelmes magyarázatait és hasznos tanácsait.

Hálával tartozom Negyedi Milánnak a berendezés fejlesztéséért és magyarázataiért. Köszönöm Kollarics Sándor és Gyüre Balázs segítségét a mérések során. Hálás vagyok Márkus Bencének, hogy bármilyen kérdéssel fordulhattam hozzá.

Köszönöm Prof. Thomas Pichlernek a lehetőséget a Bécsi Egyetemen végzett mérésekhez és Philip Rohringernek segítségét a mintakészítésben.

Köszönöm családomnak és barátaimnak a támogatást.

A dolgozat elkészítését az MTA Lendület programja támogatta a PROSPIN kutatócsoport révén, ill. az NKFIH a K119442 szerződésszám alatt.

Acknowledgments

I would like to thank my supervisor, Prof. Ferenc Simon for his help, patient explanations and useful advice.

I am grateful to Milán Negyedi for the development of the spectrometer and for his explanations in optics. I thank Sándor Kollarics and Balázs Gyüre for their help during the measurements. I would like to thank Bence Márkus for discussions and his help.

I thank Prof. Thomas Pichler for providing opportunities for the measurements at the University of Vienna. I would like to thank Philip Rohringer for his help in preparing the samples.

I am grateful to my family and friends for their support.

This work was supported by the MTA-BME Lendulet Spintronics Research Group (PROSPIN) and the Hungarian National Research, Development and Innovation Office (NKFIH) Grant Nr. K119442.

1 Introduction and motivation

Efficient light generation and light harvesting are important for sustainable economic development. Light generation is caused by the recombination of an injected electron-hole pair and light harvesting, the reverse process, involves the generation of electron-hole pair by light excitation. Essential in both processes is the strength of the interaction of the electron-hole pair and the symmetry of its wavefunction. In three-dimensional solids, the interaction is small, however, in lower dimensional materials the confinement results in stronger interactions which causes strongly bound so-called exciton states.

In the recent years, the carbon-based, lower dimensional nanomaterials e.g. single-walled carbon nanotubes (SWCNTs) have received great attention regarding the application of the light harvesting and light generation processes. It turned out that strongly bound states are found in SWCNTs because of the one-dimensionality of this kind of materials.

Understanding the spin symmetry and electron structure of these states has a great importance. The wavefunction of the exciton has one singlet and three triplet states according to the spin, although the optically active processes, which are important for the application, occur only between the singlet states. Because their formation probability is low, the triplet excitons are long-living, their decay is a slow process, which hinders the optical applications of SWCNTs.

The optically detected magnetic resonance (ODMR) is a suitable method for investigating the energy and spin structure of the excited singlet and triplet states. SWCNTs have a particular property that the optical transition energies depend on the geometry of the nanotube significantly. Therefore the ODMR measurements have to be analyzed according to the wavelength of the excitation and emitted light.

In this MSc Thesis, I used the ODMR method for investigating the optical properties of SWCNTs. First of all, I present the preparation of the samples used for the measurements, then I discuss some important physical properties of the so-called ODMR maps, which was measured earlier by Milán Negyedi. I determine the chirality dependent singlet-triplet gaps of the nanotubes and I interpret a new phenomenon, the behavior of bundle peaks on the ODMR maps.

2 Theoretical background

2.1 Photoluminescence

Luminescence is a generic process in nature that involves all light emitting processes. There are several variants of luminescence, which are classified according to the method of the excited state generation, which emits lights. We therefore find among others e.g. chemi-, electro-, mechanical-, photo-, radio-, and thermoluminescence.

Photoluminescence is a light emitting process which occurs after a photon is absorbed by a molecule or an atom. The possible processes, which can follow the excitation, are illustrated in Figure 1. This is the so-called Jablonski diagram which depicts the electronic states of a molecule and the transitions between them. The radiative transitions are marked by continuous arrows and the non-radiative ones are illustrated by dashed lines.

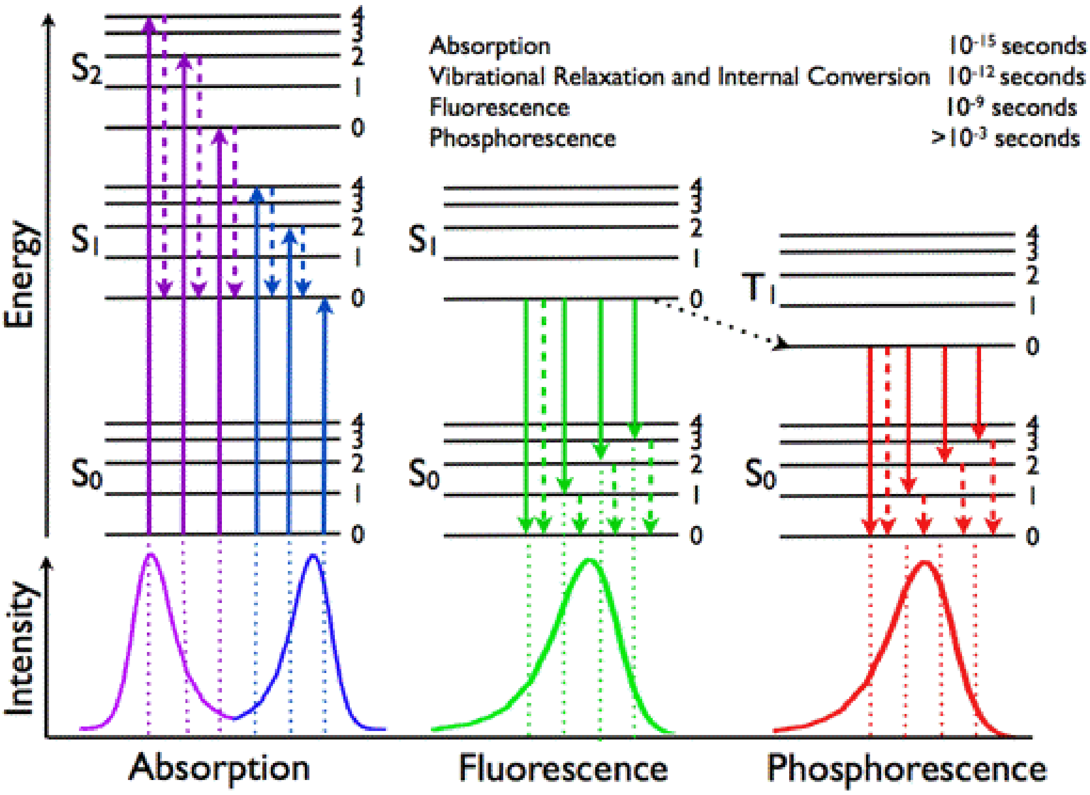

Figure 1: Jablonski diagram of a typical photoluminescent system. S and T denote singlet and triplet levels, respectively. The typical lifetimes of the different processes are also given. [25]

First of all, absorption is shown in the first column where an electron goes from the S_0 singlet ground state to a higher energy level and excited singlet states are created denoted by S_1 and S_2. A singlet state is an electronic state in which the total spin is zero. In a triplet state, the total spin of the electrons is $S = 1$. From ground state, the electrons can form a singlet or a triplet state as well. Since forming a triplet state involves a forbidden spin transition, it is more probable to form a singlet excited state.

Following absorption, the molecule reaches a vibrational level of an excited state. Since this level may not be in thermodynamic equilibrium, the molecule can undergo vibronic changes before radiating a photon. This so-called *vibrational relaxation* (VR) process means that the energy of the excited vibrational mode is transformed into the energy of the kinetic modes of the molecule and the excited electron-hole pair relaxes to a lower vibrational level. Another non-radiating process is the *internal conversion* (IC), which is a transition to a lower excited state of the molecule. In this case, the molecular spin state remains the same and some of the energy of the excited state is transformed.

Regardless of which state is reached during the excitation, the electron moves into the lowest possible energy level. That is to say that the photoluminescent radiation happens always from the lowest vibrational level of the lowest excited state to one of the vibrational levels of the ground state. This is the so-called Kasha's rule.

The emission of light from the lowest excited singlet state is known as *fluorescence* (PL). However, there are additional ways for the decay of the excited state. It can occur that the singlet state passes to a triplet state without light emission which process is called *intersystem crossing* (ISC). This non-radiative deexcitation is forbidden in first order due to the spin-flipping. Because the unpairing of the spins can occur only if it is made possible by spin-orbit coupling, in which the magnetic field arising from the orbital motion of the two electrons interacts with the spin magnetic moments.

If the deexcitation happens from that excited triplet state to the singlet ground state, this kind of radiation is called *phosphorescence.* As this is forbidden transition, the lifetime of the phosphorescence is 6-8 orders of magnitudes longer than fluorescence and this is the slowest form of relaxation.

We continue the discussion with the photophysical properties of the studied materials following an introduction to the material properties.

2.2 Fundamentals of carbon nanotubes

2.2.1 Structure and geometry

The carbon nanotubes are intensively studied due to their fundamental properties and potential applications. This kind of nanomaterials has a quasi one-dimensional structure causing unique electronic, optical and chemical properties which are beneficial in light harvesting and generation.

We distinguish many types of nanotube structures such as multi-walled carbon nanotubes (MWCNTs), which have multiple layers [1], or single-walled carbon nanotubes (SWCNTs), nanotubes with a single layer [2], [3]. In this thesis, I write only about the single-walled carbon nanotubes and refer to them as nanotubes.

The best way to imagine the geometry of carbon nanotube is to consider it as a rolled up stripe which is cut out from a graphene sheet. For understanding this picture, first, we need to define the chirality or Hamada-vector of graphene [4]. Here, $\mathbf{a}_1$ and $\mathbf{a}_2$ are the basis lattice vectors of the graphene.

$$\mathbf{C}_{n,m} = n \cdot \mathbf{a}_1 + m \cdot \mathbf{a}_2 \qquad 0 \leqslant n \leqslant m \quad n, m \in \mathbb{Z} \tag{1}$$

Along this two-dimensional vector, the sheet is cut and rolled up that the end points overlap and the length of the vector become the circumference of the nanotube (Figure

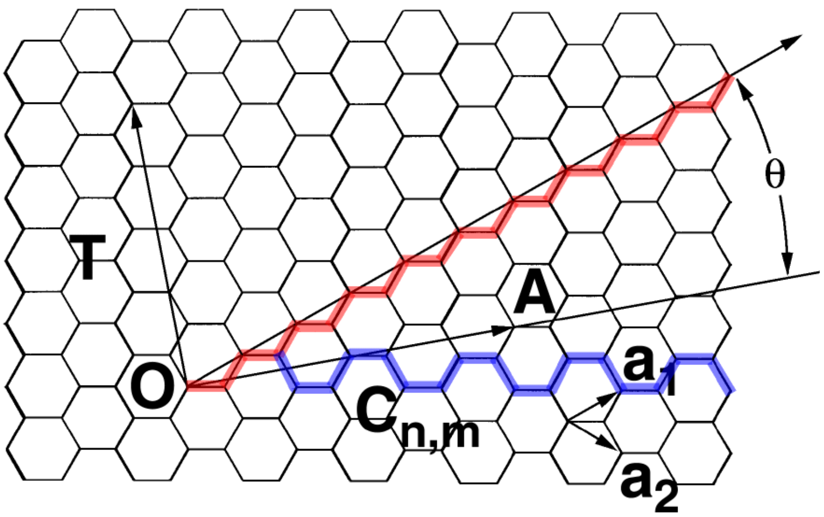

Figure 2: Demonstration of the geometry of carbon nanotubes on a graphene sheet. The blue line is the chirality of the armchair nanotube and the red line is the chirality of the zig-zag nanotube. T denotes the tube axis. [6]

2). Chirality is used for describing and characterizing the nanotubes since one can assign a value of (n, m) to each nanotube. According to (n, m) one can distinguish special cases of nanotubes: an *armchair* nanotube is observed when $n = m$ and *zig-zag* when $m = 0$. Otherwise, the nanotubes are chiral, in other words, they do not have a superposable mirror image [7].

From the chirality, one can calculate the diameter of the nanotube with the following formula, where $a_0 = 0.2461\,\mathrm{nm}$ marks the length of the carbon-carbon bond.

$$d = \frac{a_0\sqrt{n^2 + m^2 + n \cdot m}}{\pi} \tag{2}$$

In a real sample, the diameters of the chiralities show a Gaussian-distribution [7]. Although this distribution is not continuous, because (n, m) can be only discrete in the grown single-walled carbon nanotubes. Recently a new chirality selected growing method is demonstrated, which makes possible to create samples with one type of nanotubes in it [8].

As a result of the van der Waals forces, the nanotubes are not able to remain separated, they are settled in bundles.

2.2.2 Electrical and optical properties

The electrical structure of single-walled carbon nanotubes is originated from graphenes. The electronic band structure of the graphene is presented by Figure 4. The graphene is a zero-gap semiconductor, whose valence and conduction band meet at the K point of the Brillouin zone.

The quasi-one-dimensional structure of the nanotubes gives a condition for the possible states. Discrete states are found in the direction of the k-space perpendicular to the length

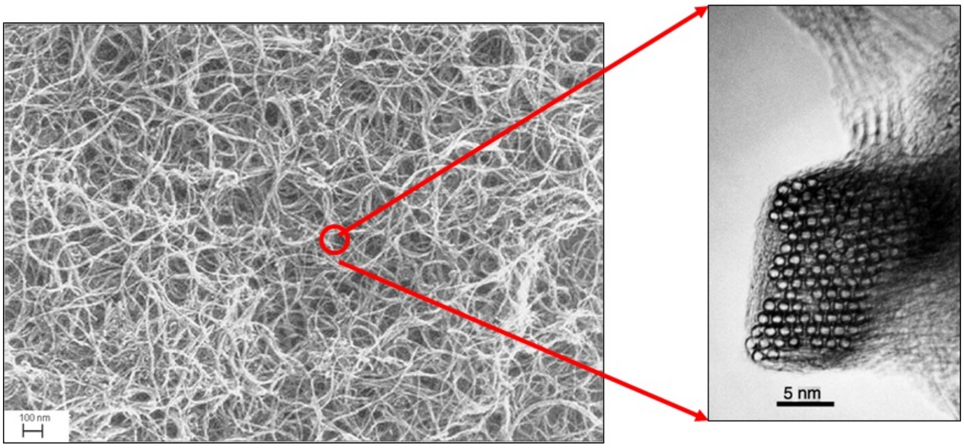

Figure 3: *Electron microscopy image of an SWCNT sample, which shows the presence of bundles.* [14]

of the tube in real space. Since the wavefunction cannot change shifted by **C** thus it gives periodic boundary condition on the electron wave function for the possible k wavenumbers.

$$e^{i\underline{k}\,\underline{C}} = 1 \tag{3}$$

According to this condition, the allowed k vectors can be only the lines perpendicular to the chirality. If these lines intersect the K point of the Brillouin zone, then the conduction and valence band meet and the nanotube does not have a gap between the conduction and valence bands. Such SWCNTs are called metallic. Knowing the chirality it can be calculated easily whether the nanotube metallic or semiconducting following a simple rule. The nanotube with (n, m) chirality is metallic if $n-m$ is divisible by 3 and semiconducting otherwise (Figure 5). It also means that in a real sample the rate of the metallic and the semiconducting nanotubes is about 1:2 and these nanotubes are present randomly in bundles.

If we know the dispersion relation, the density of states - the number of states per interval of energy - can be calculated.

$$\rho(E) = \frac{dN(E)}{dE} = 2\sum_{\underline{k}i} \delta(E - E_i(\underline{k})) = \frac{2V_d}{(2\pi)^d} \sum_i \int d^d k \delta(E - E_i(\underline{k})) \tag{4}$$

According to the above equation, the density of states is proportional to the reciprocal of the wavenumber derivative of the energy in one-dimensional systems.

$$DOS \equiv \rho(E) \sim \left(\frac{dE}{dk}\right)^{-1} \tag{5}$$

Figure 6 presents the energy of a metallic and a semiconducting nanotube. Here, we find that the dispersion relation has a parabolic behavior beside the linear areas. Therefore the function has local extrema at some points where the derivative is zero. It follows that DOS diverges at the extrema and typical peaks are observed symmetrically to the Fermi energy. These peaks are called Van Hove singularities [6].

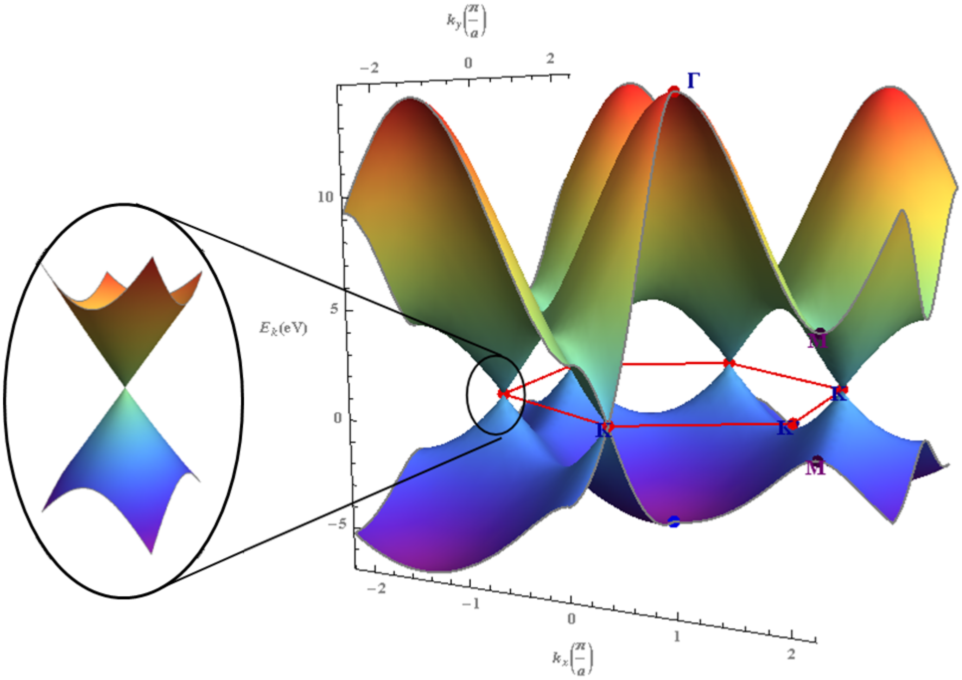

Figure 4: The electronic band structure of graphene. The vicinity of the K points, where the two bands touch, is shown enlarged.[13]

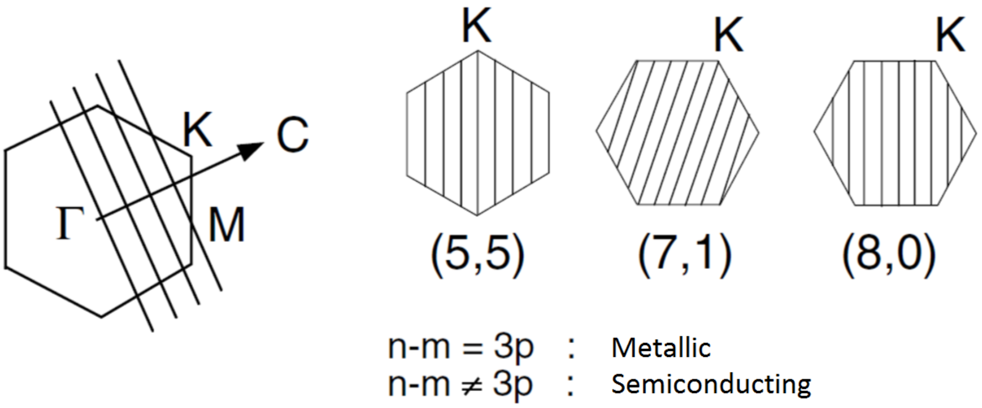

Figure 5: Brillouin zone of graphene with the possible states of nanotubes for a few (n, m) indices. [10]

Van Hove singularities have a great importance for the optical investigation of single-walled carbon nanotube because the optical transition can occur only between two of them due to the high DOS. These singularities are labeled symmetrically to the Fermi energy and the corresponding optical transitions from the ith singularity of the valence band to the jth singularity of the conduction band are denoted by E_{ij}. Along the circumference of carbon nanotubes, quantized electron states are found which have a well-defined angular momentum. This means that for the interaction of light one has to consider selection

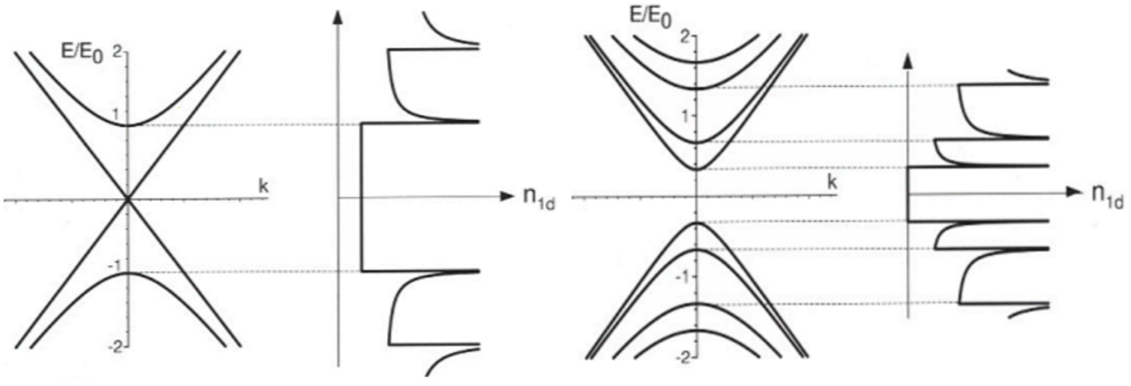

Figure 6: Dispersion relation and density of states of the metallic and semiconducting nanotubes. Note the presence of the Van Hove singularities at the extrema of the bands.

rules because the z component of the angular momentum of light can be also $m = 0, 1, -1$ depending on the polarization.

When light is polarized along the axis of the nanotube, the z-component of the angular momentum cannot change and only the transitions between the states with the same m are allowed. E_{ii} transitions can occur with this condition. When light is perpendicular to the axis of the nanotube, the change of the z component of angular momentum is $\Delta m = \pm 1$ and transition with $E_{ii\pm1}$ energy can happen. However, this second process is much weaker than the first one due to the effect that the E field involves charge density along the nanotube which shields the external field.

One can calculate the energy of the ith optical transition for metallic and semiconducting nanotubes by applying the tight-binding model [11].

$$E^m_{ii} \approx i \cdot \frac{0.85\ [eVnm]}{d\ [nm]} \tag{6}$$

$$E^s_{ii} \approx i \cdot \frac{2.55\ [eVnm]}{d\ [nm]} \tag{7}$$

It means that energy of an optical transition depends on the geometry of the given nanotube and the Van Hove singularity from which the excitation happens. We note that Equation 6-7 are only valid in the first neighbor tight-binding approximation. For a realistic case, deviations are observed from this simple reciprocal relation, which is discussed further below.

One important thing to consider that the semiconducting nanotubes have a gap of states between the singularities and the metallic ones have a continuous density of states because the valence and the conducting band about.

From the study of Figure 7, one can see that photoluminescence measurements are only measurable for semiconducting nanotubes. Since the valence and conducting bands touch each other in metallic nanotubes, the excited quasiparticle can move toward zero energy through internal relaxation and thus no photon emission occur.

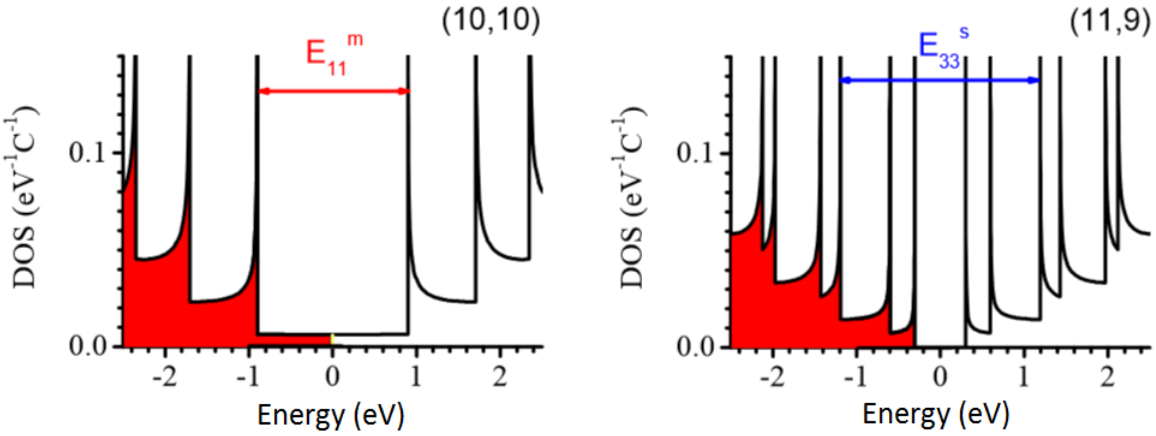

Figure 7: *Density of states for (10,10) metallic and (11,9) semiconducting single-walled carbon nanotubes calculated in tight-binding model. Van Hove singularities are found symmetrically to the Fermi energy. In the figure, one can see the* E_{11}^m *and* E_{33}^s *optical transitions as an example. The red area denotes the occupied states.* [24]

2.2.3 Photophysics of single-walled carbon nanotubes

Photoluminescence can be realized in SWCNTs in several ways. It is important to mention that one has to investigate individual nanotubes for observing these different processes. Due to the arrangement of bundles, the semiconducting nanotubes may have a metallic neighbor thus photoluminescent signal can not be observed since the excited state can deexcitate non-radiatively. This is called photoluminescence quenching [16].

Individualization of nanotubes is performed by surfactants, molecules dissolved in water, which reduce the surface tension. These molecules have a polar and an apolar part, therefore they are able to envelop the nanotubes and create a micell as it is shown in Figure 8. A few nanotubes may still stick together, but this process can prevent the formation of bigger bundles [16].

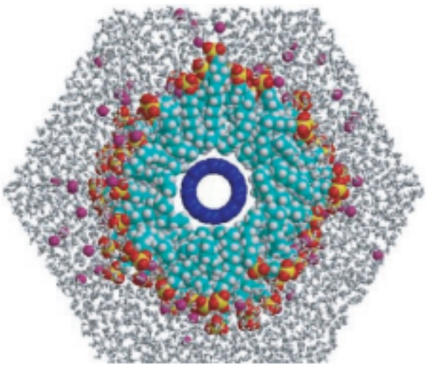

Figure 8: *Sodium dodecyl sulfate (SDS) molecules individualize a nanotube. On this picture the nanotube is marked by blue, the polar and apolar part of the SDS molecule are denoted by red and turquoise. The water is gray.* [16]

Exciton

In the simplest photoluminescence process, the nanotube absorbs a photon and an electron-hole pair is generated. This, according to the Kasha rule, moves to the lowest possible state of energy where the photon emission takes place. The lowest energy state is a Van Hove singularity, which is well-defined for every nanotube, so a nanotube always emits a photon at the same wavelength. This process is illustrated in Figure 9.

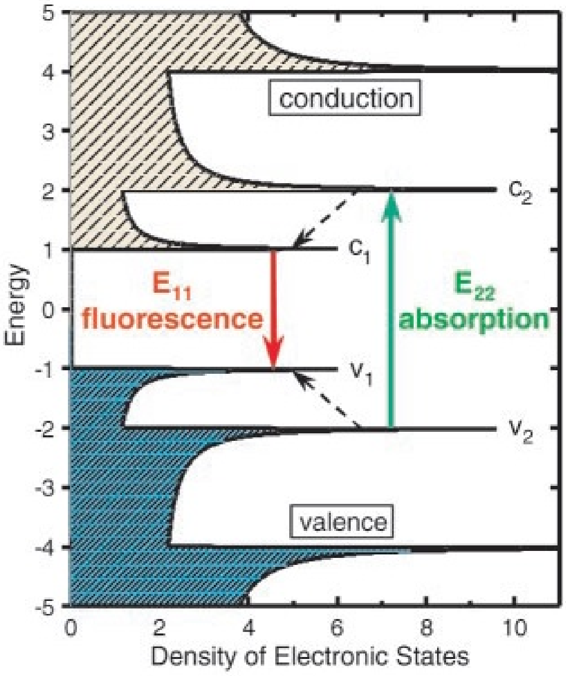

Figure 9: *Photoluminescence of single-walled carbon nanotubes. The optical transition with* E_{22} *energy is excited and a photon with* E_{11} *energy is emitted. The dashed lines denotes the internal relaxation of the electron and the hole.* [5]

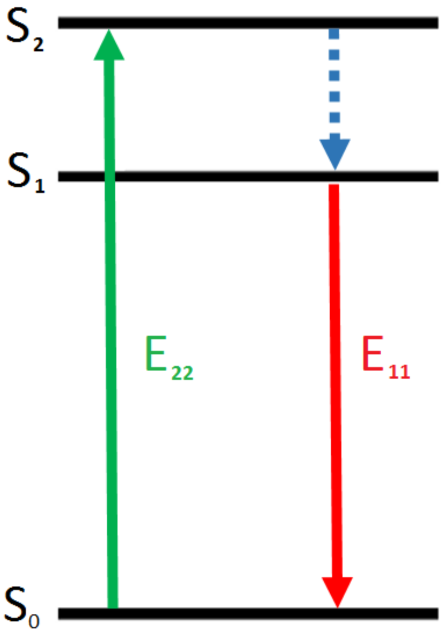

Figure 10: *Photoluminescence of single-walled carbon nanotubes considering excitons. The nanotube is excited to the* S_2 *state, then the emission occurs from the lowest possible state.*

Later work proved that during optical excitation of nanotubes strongly correlated electron-hole states are produced which is called exciton [19]. Creating such a quasiparticle, an electron is excited from the valence band to the conducting band. Attractive Coulomb-force acts between the oppositely charged particles, which appears as a long-range, strong interaction. Owing to this interaction bound state evolves between the electron and the hole. The light absorption and creation of exciton are shown in Figure 10.

The wavefunction of this quasiparticle is spatially localized, however, its motion along the tube axis is allowed (Figure 11).

Due to the electron-hole interaction, hydrogen-like, so-called Rydberg series of exciton states are evolved [19]. It was shown in Ref. [19] that single photon excitations only allow transition to the lowest 1*s* exciton due to the optical selection rules. However, nonlinear processes, such as a multi-photon excitation allows the excited excitonic states. Figure 12

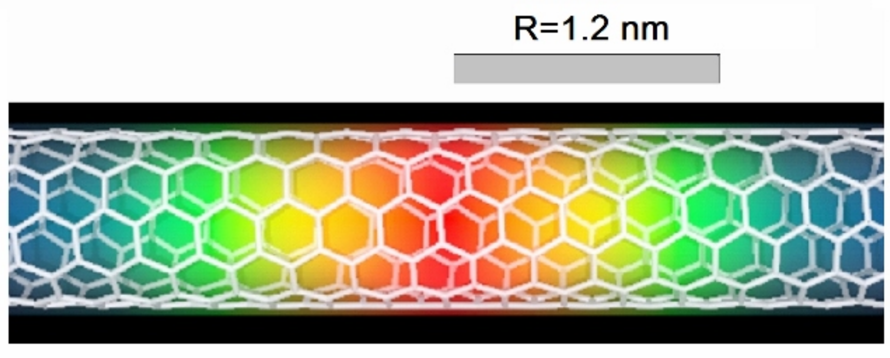

Figure 11: *Density of the envelope function of the 1s exciton. The density expresses the finding probability of the electron and the hole, the distance, denoted by R, represents the half-width of the exciton.* [19]

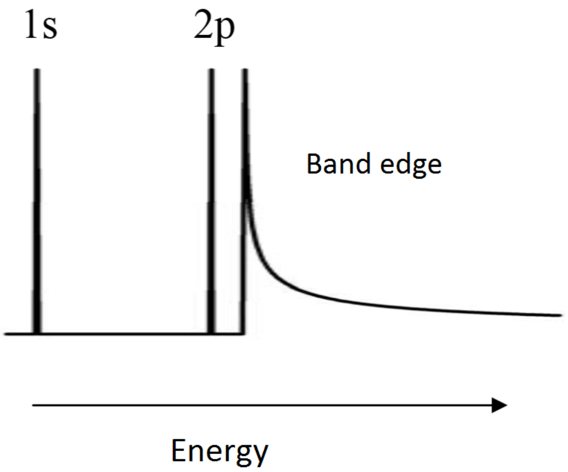

Figure 12: *DOS of SWCNT in a presence of an exciton.*

shows the energy of $1s$ and $2p$ states in addition to the DOS associated with the carbon nanotube single-electron band structure. The energy difference between such a state and the band edge is the binding energy of the exciton, which is found to be about 400 meV for semiconducting SWCNTs [19]. We note that this is an exceptionally large value, in three-dimensional solids, the typical binding energies are a few meV.

The quasi-one-dimensional structure causes this bound state since the two particles are not able to separate from each other like it can happen e.g. in a crystal. They move together until they can recombine.

PL map of SWCNTs

In the case of photoluminescence spectroscopy, the emission spectrum of nanotubes is measured at several excitation wavelengths. Such a measurement is shown in Figure 13. On this photoluminescence map, one can see several peaks, each of them belongs to a particular chirality. We note that the explanation of the peak positions in the PL map already involves various effects such as the ”beyond first neighbour tight-binding

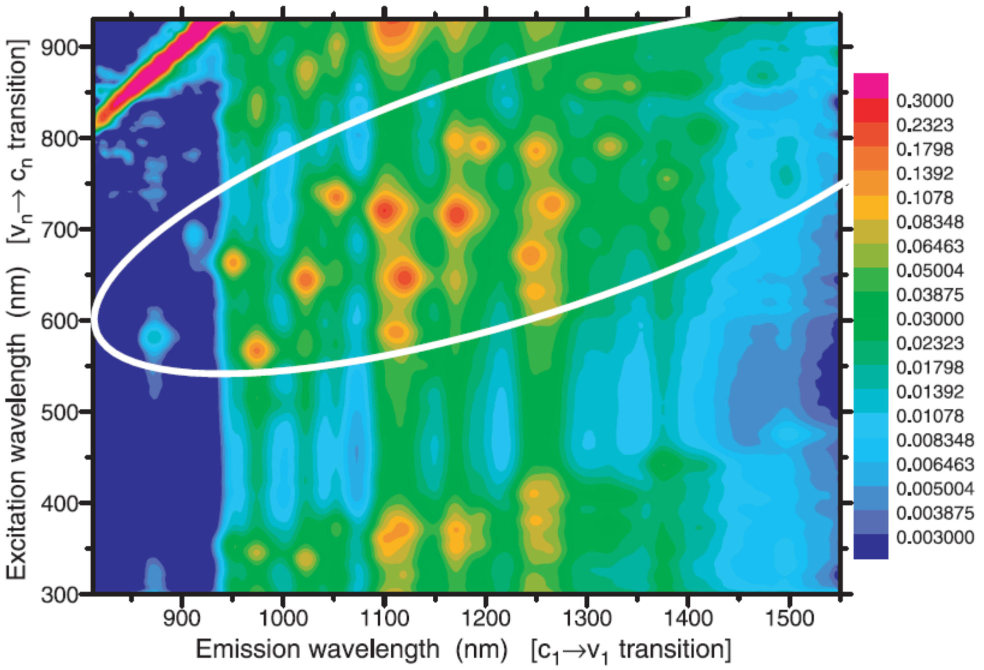

Figure 13: Photoluminescence map of single-walled carbon nanotubes.[5]

approximation" and the presence of excitons. While theoretical works are known which could explain the actual peak positions, it is customary in experimental work that the identified peaks in the PL map are considered further as an empirical input. This is followed herein, too.

Here, the emission wavelength is clearly defined. The vertical lines in the figure are originated from the experience that several excitation wavelengths belong to one emission wavelength. It can happen that the nanotube is excited by more energy than the 2^{nd} optical transition and the plus energy is removed by vibrational relaxation during a phonon emission or by internal conversion.

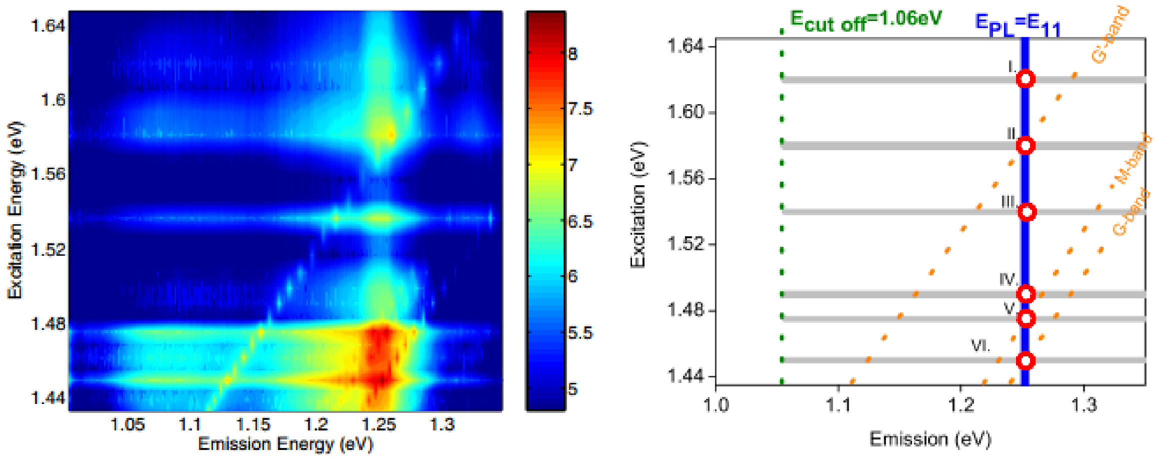

Figure 14: *Photoluminescence map with a line originating from Raman-scattering.*[12]

If the photon is not absorbed by the molecule but is inflexibly scattered while polarizing the electron cloud, the process is called Raman scattering. In the course of photoluminescence measurement, this process can also occur and one can detect the scattered light as well. For carbon nanotubes, we find resonance peaks from typical Raman scattering at certain energies which appear on the photoluminescence map as lines with different slopes. If such a Raman line passes through a chirality peak i.e. the energy from the resonance is equal to the energy of the E_{11} optical transition, the measurable signal is amplified [12]. Figure14 shows the related measurement results from Ref. [12].

2.3 Optically detected magnetic resonance

Optically detected magnetic resonance (ODMR) is a double resonance technique which combines optical measurements with magnetic resonance spectroscopy. ODMR uses the advantageous properties of both methods: the high energy resolution of the magnetic resonance and the high sensitivity of the optical measurements.

Application of magnetic field causes a modification in the populations of the spin sublevels of a triplet state. It makes changes in the optical properties of the system and this change can be detected during the measurements.

Basic principles

The basic ODMR process is illustrated in Figure 15. In the course of ODMR measurement, $S_0 \rightarrow S_1$ transition is pumped by a laser which causes a steady-state population of the triplet sublevels. The probability of the intersystem crossing is denoted by k_{ISC}. In the case of this example, the population rates (p_u) and decay rates (k_u) are not the same, therefore the relative populations of the sublevels are also different (n_u).

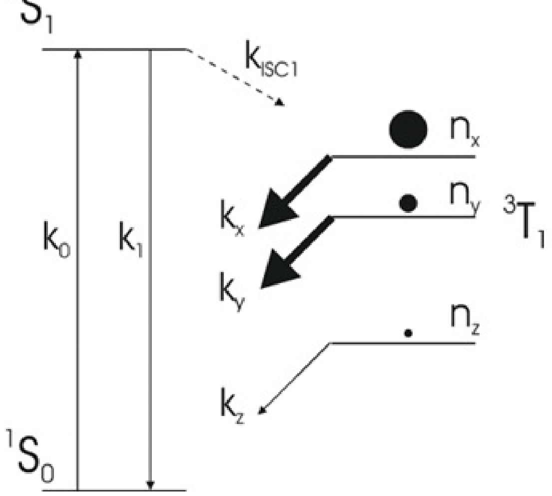

Figure 15: Scheme of the triplet states under continuous illumination. The size of the arrows and the circles indicate the differences between the populations (n_u) and the decay rates (k_u) of the sublevels. [23]

If one applies resonant microwaves, transitions are possible between any two sublevels e.g. T_x and T_z, which have the largest population difference in this example. After the changes of the population caused by the resonant microwave, the T_z state has more population, however, its decay rate remains the same i.e. the smallest (Figure 16). It means that more electrons stay in the triplet state per unit time, therefore fewer electrons can deexcite to the ground state and can be excited again to the S_1 state. This process causes the decrease of the photoluminescence signal [22], [23].

To study the change of the photoluminescence signal, we need to analyze the rate equation of the population of the states which are involved in the process [23]. The total number of excitable electrons is denoted by N.

$$N = [S_0] + [S_1] + \sum_{u=0}^{3} [T_u] \tag{8}$$

Here, the population of the ground state is $[S_0]$, the excited singlet and triplet states are indicated by $[S_1]$ and $[T_u]$.

For the following calculation of the population dynamics of the five sublevels, we need to suppose a few conditions. First of all, that no spin-lattice relaxation occurs between the triplet states, which is possible at low temperatures, and they do not affect the population of the other two sublevels. Another condition, that due to the short lifetime of the S_1 level, the population of this state is negligible.

$$N \approx [S_0] + \sum_{u=0}^{3} [T_u] \tag{9}$$

The differential equations of the population dynamics are described by the following equations:

$$\frac{\mathrm{d}[S_0]}{\mathrm{d}t} = -k_0[S_0] + k_1[S_1] + \sum_{u=0}^{3} k_u[T_u] \tag{10}$$

$$\frac{\mathrm{d}[S_1]}{\mathrm{d}t} = k_0[S_0] - k_1[S_1] - \sum_{u=0}^{3} k_{ISC} P_u [S_1] = k_0[S_0] - k_1[S_1] - k_{\mathrm{ISC}}[S_1] \tag{11}$$

$$\frac{\mathrm{d}[T_u]}{\mathrm{d}t} = k_{\mathrm{ISC}} P_u [S_1] - k_u[T_u] \tag{12}$$

Here, P_u denotes the relative populating probabilities ($P_x + P_y + P_z = 1$), from which the population rates of the sublevels are determinable: $p_u = P_u k_{ISC}$. From the above equations, the population of the triplet states is calculated:

$$[T_x] + [T_y] + [T_z] \sim \frac{p_x}{k_x} + \frac{p_y}{k_y} + \frac{p_z}{k_z} \sim n_x + n_y + n_z \tag{13}$$

In the presence of microwave field, which saturates the $T_x - T_y$ transition, the population and the decay rates change in first approximation:

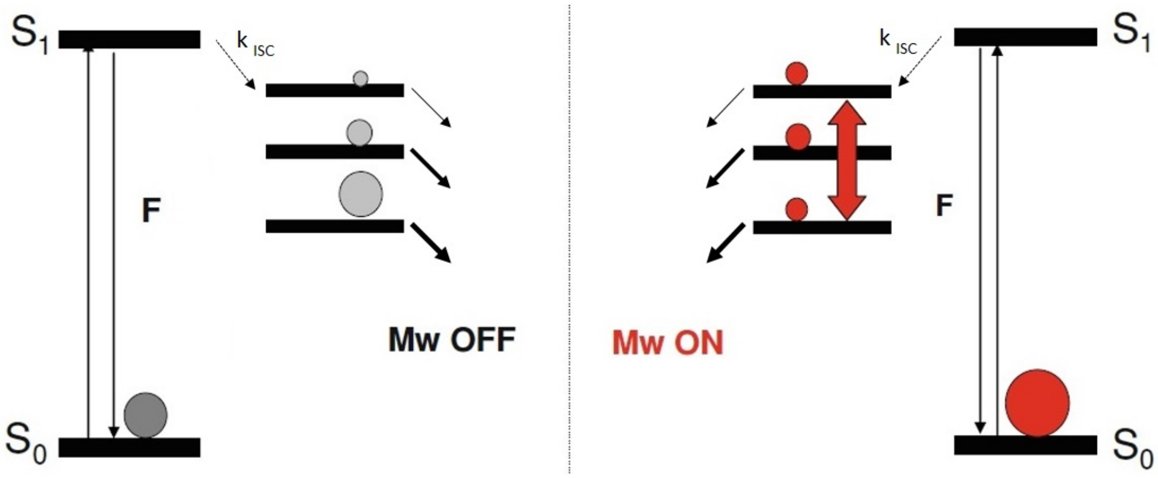

Figure 16: *The principle of ODMR spectroscopy. Resonant microwave field (Mw) induces the change of the triplet sublevel population.*[22]

$$\begin{aligned} p'_x &= \frac{1}{2}(p_x + p_z) \\ p'_y &= p_y \\ p'_z &= \frac{1}{2}(p_x + p_z) \end{aligned} \tag{14}$$

$$\begin{aligned} k'_x &= \frac{1}{2}(k_x + k_z) \\ k'_y &= k_y \\ k'_z &= \frac{1}{2}(k_x + k_z) \end{aligned} \tag{15}$$

And the population of the triplet state under continuous illumination of microwave field is:

$$[T_x]' + [T_y]' + [T_z]' \sim \frac{p_x + p_z}{k_x + k_z} + \frac{p_y}{k_y} + \frac{p_z + p_x}{k_z + k_x} \tag{16}$$

The fluorescence intensity is related to the $[S_0]$, therefore the change of the signal is proportional to the change of the population of the S_0 state, which one can express using the condition that the population of the S_1 state is negligible (equation 9).

$$\Delta[S_0] = [S_0]' - [S_0] = -\Big(\sum_{u=0}^{3}[T_u]' - \sum_{u=0}^{3}[T_u]\Big) = -\Delta\Big(\sum_{u=0}^{3}[T_u]\Big) \tag{17}$$

Equation 17 indicates that a decrease of triplet population leads to the increase of the PL signal. This is easy to understand if one thinks through that the molecules, which are trapped in long-living triplet states, are liberated and can participate in the fluorescence cycle again. With ODMR spectroscopy this change can be measured. This measurement is realized in practice by applying an amplitude modulated (or chopped) strong microwave and the resulting optical signal is detected using a lock-in detection.

$$\Delta\Big(\sum_{u=0}^{3}[T_u]\Big) \sim \frac{1}{k_x + k_z}(n_x - n_z)(k_x - k_z) \tag{18}$$

ODMR on single-walled carbon nanotubes

The ODMR process on nanotubes is illustrated in Figure 17. First, the absorption of light generates an exciton to the energy level proportional to the second optical transition, then it relaxes to the lowest possible excited state because of Kasha's rule. Here, it can recombine and emit a photon with k_{10} probability, which contributes to the fluorescence signal. This path is illustrated by the red arrow.

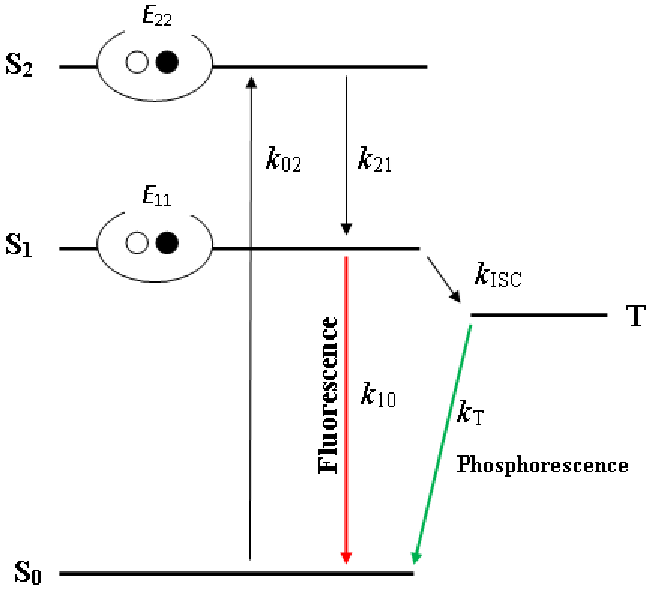

Figure 17: Jablonski diagram for single-walled carbon nanotubes.

However, from S_1 state, it can cross over to the triplet states with k_{ISC} decay rate. The deexcitation from this sublevels is denoted by the green arrow. If the system is irradiated by microwaves radiation, after aligning the differences between the sublevels with magnetic field, then the strength of the phosphorescence signal changes. It causes the increase (or decrease) of the population of the S_0 ground state. The strength of the fluorescence signal depends on the population of the ground state since the greater population let participate more nanotubes in the fluorescence cycle.

This small change can be detected. The $T_1 \rightarrow S_0$ transition is 3-4 magnitudes smaller than the $S_1 \rightarrow S_0$ fluorescence signal. To measure ODMR, signal-to-noise ratio of the PL measurement has to be at least this difference.

Separation of the three sublevels

In the absence of magnetic field, the triplet states could be degenerate. However, due to the presence of unpaired electrons in the system, there is magnetic dipole–dipole interaction between the spins which causes the separation of the three sublevels. This effect is called zero field splitting. The strength of the interaction depends on the symmetry of the measured system.

The separation is described by the spin Hamiltonian:

$$H_{\mathrm{ZFS}} = \mathbf{SDS} \tag{19}$$

Where **S** is the total spin angular momentum and **D** is the dipolar interaction tensor. After diagonalization of the tensor, equation 19 can be rewritten in the following form:

$$H_{ZFS} = D\Big(S_Z^2 - \frac{1}{3}S(S+1)\Big) + E(S_X^2 - S_Y^2) \tag{20}$$

Here, S_x and S_y are the x- and y- components of the total spin after diagonalization, in the principal axes system. D and E are the axial and the transversal components of the magnetic dipole-dipole interaction. They are the parameters of the splitting and determine the distance between the energy of the sublevels [21].

Due to these parameters depend only on the average of the spatial coordinates of the electrons, D and E show the structure and symmetry of the molecule. The ZFS can also originate from the electrostatic interaction between the spin levels and the surroundings except for a spin-half system.

In the presence of a magnetic field, the Zeeman effect dominates and the triplet states are separated with different magnetic spin. The splitting is described by the corresponding Hamiltonian:

$$H_{\mathrm{Z}} = g\mu_{\mathrm{B}}\mathbf{SB} \tag{21}$$

Where μ_{B} is the Bohr-magneton, g is the g-factor, **S** is the total spin and **B** is the external magnetic field. The eigenenergies are defined by the above equation where m is the z component of the spin that can be $m = -1, 0, 1$.

$$E_{\mathrm{Z}} = mg\mu_{\mathrm{B}}\mathbf{B} \tag{22}$$

For a triplet system, the transition energy can be calculated from the eigenenergy of the three sublevels with the $\Delta m = \pm 1$ transitions as only these transitions are allowed in first order in magnetic resonance experiments. The equation 23 gives the frequency condition for the transitions between the spin states.

$$\Delta E = g\mu_{\mathrm{B}}\mathbf{B} = h\nu_{\mathrm{resonance}} \tag{23}$$

3 Experimental methods

3.1 Photoluminescence spectroscopy

Optical spectroscopy is a suitable method to analyze the optical transitions of SWCNTs. In the case of photoluminescence (PL) spectroscopy, nanotubes are excited by a monochromatic light, then the emission spectrum is measured as a function of wavelength.

In our measurements, a home-built spectrometer is used which has several advantages compared to a commercial one. Figure 18 is a schematic presentation of the experimental setup.

3.1.1 Optical setup of the home-built spectrometer

The light sources of the spectrometer are two tunable lasers, which are pumped by a frequency doubled Nd:YAG laser with 532 nm (*Coherent Verdi 5G*). To cover the desired wavelength range, we used a Ti:Sapphire and a dye-laser (*Radiant Dyes GmbH*) with a series of dyes (Rhodamin 101, Rhodamin 6G, DCM Special, Pyridine 1-2). It allows to perform measurements between 560 and 900 nm. Selection of the wavelength occurs by a Lyot-filter, which is built into the laser.

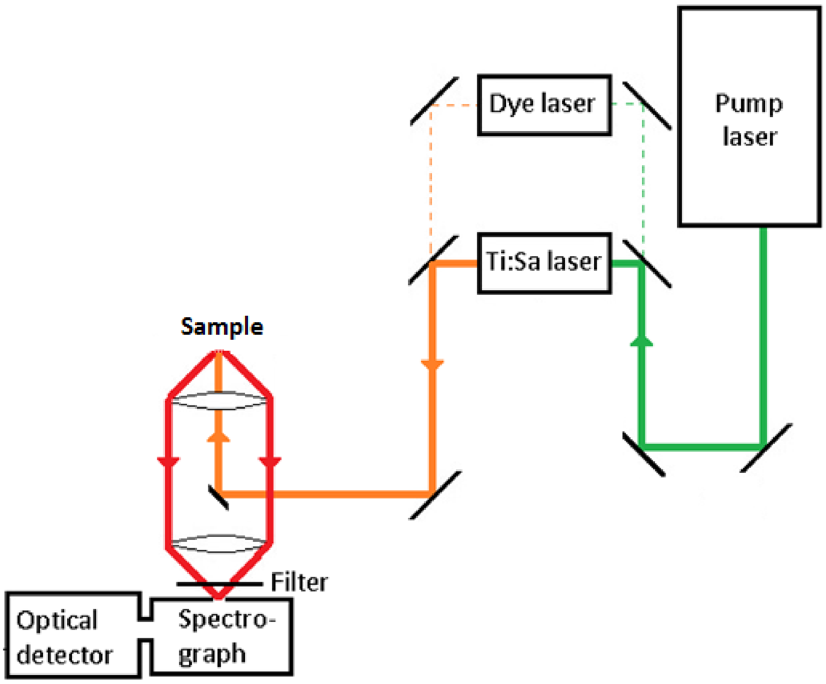

Figure 18: Schematic diagram of the home-built spectrometer. The colors of green, orange, and red represent the 532 nm pump, the 560-900 nm exciting laser, and the 1000-1500 nm scattered light, respectively. Arrows show the direction of the light propagation.[20]

The light emitted from the tunable laser is first driven by high reflecting dielectric coated mirrors to a small right angle prism mirror, which is responsible for making the light parallel to the axis of the spectrometer. Thus, we get an arrangement of a so-called 180° geometry. An achromatic doublet lens (*Thorlabs Inc. "AC254-030-B"*) follows the prism, which has a function both focusing the excitation and collecting the scattered light. We used this kind of lens to eliminate the chromatic aberration, i.e. the wavelength dependence of the refractive index, which might become significant in the measured wavelength range. The achromatic doublet lens has also a smaller spherical aberration than a comparable spherical singlet lens.

Finally, another lens focuses the collimated beam on the entrance of the spectrometer. The f-number of this lens fits the f-number of the spectrograph, which is, in this case, $f/\# = 4.1$.

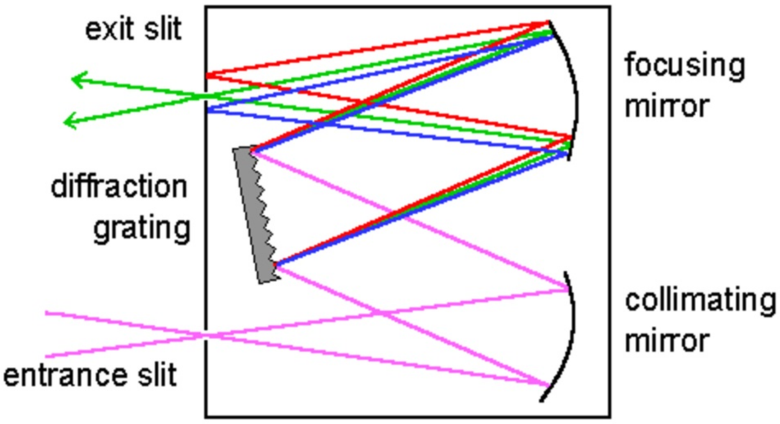

Figure 19: The Czerny-Turner spectrograph. The entrance is in the focal point of the first concave mirror, so a collimated beam is led from the mirror to the plane diffraction grating. This element separates the light according to wavelength. The light goes still collimated to the second concave mirror, which is in the focal point of the output aperture. [26]

In order to get rid of the disturbing signals such as e.g. quasi-elastic scattered light (or Rayleigh-light), a long-pass interference filter was placed before the entrance (*Thorlabs "FEL900"* and *Thorlabs "FELH0800"*).

Measurements are made at 77 K, thus the sample is cooled to this temperature: the quartz tube containing the SWCNTs sample is placed in a cryostat filled with liquid nitrogen. However, this process involves the formation of bubbles, which may cause problems in detecting the emitted signal. In order to eliminate the bubbles, the sample holder is fixed with vacuum grease to the cryostat wall. This arrangement, due to the double glass, makes it difficult to focus and it also slightly reduces the detected signal intensity.

After the filter, a single-channel *Jobin Yvon iHR320* spectrometer follows, in this case in a traditional Czerny-Turner configuration. Here, a grating disperses the incoming light by wavelength and a concave mirror passes it to the output aperture. We used a one-channel spectrometer, therefore the measured wavelength is guided to the detector by rotating the grating. Detection can also be accomplished using a diode array, where diffuse light divided by wavelength arrives at the detector and no rotation of the grating is required. A liquid-nitrogen cooled InGaAs photodiode is used to detect the photoluminescence signal.

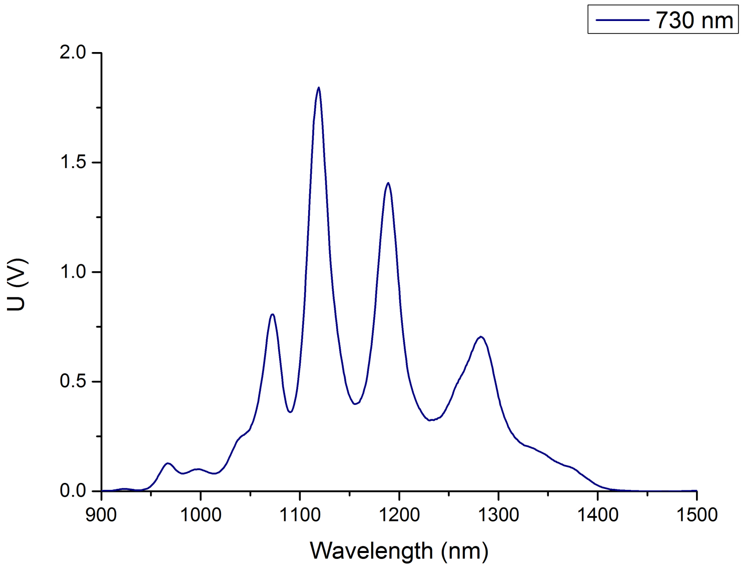

Figure 20: Photoluminescence spectrum of SWCNTs measured by our home-built spectrometer at 730 nm excitation wavelength. The data are normalized to 100 mW excitation power and the baseline is substracted.

In PL-measurement first, the wavelength is selected by rotating the Lyot filter with 1 nm accuracy and measured by an *Avantes AvaSpec 2048* spectrometer. The emission spectra of nanotubes show well-separated peaks, as is illustrated in Figure 20. These peaks belong to the chirality of several carbon nanotubes in the given sample. The spectra are measured by changing the wavelength of the laser in 3 nm steps then they are interlaced forming a PL map.

3.1.2 Comparison with a commercial spectrometer

We compare our instrument with a commercial photoluminescence spectrometer (*Horiba Jobin Yvon, Fluorolog*).

The first difference between the two types of development is the light source. The home-built spectrometer has tunable lasers for excitation, on the other hand, the conventional version uses a 450 W Xenon lamp. With laser, one can achieve approximately 100 mW intensity light on the sample. With the Xenon lamp, only 1 mW power is achievable for a 1 nm excitation bandwidth due to the double monochromator which filters the output light. There is no difference in the resolution of the exciting light, in both cases, we can determine the wavelength of the excitation light with 1 nm precision.

Detection takes place in both cases with an InGaAs photodetector. The difference between the two construction is that our instrument does the measurements with 1 pixel, in contrast to the FluoroLog which has a diode array with 1024 pixels.

It means that the diode array needs less time to achieve the same signal-to-noise ratio since it can collect more photon. The detection of photons is described by Poisson

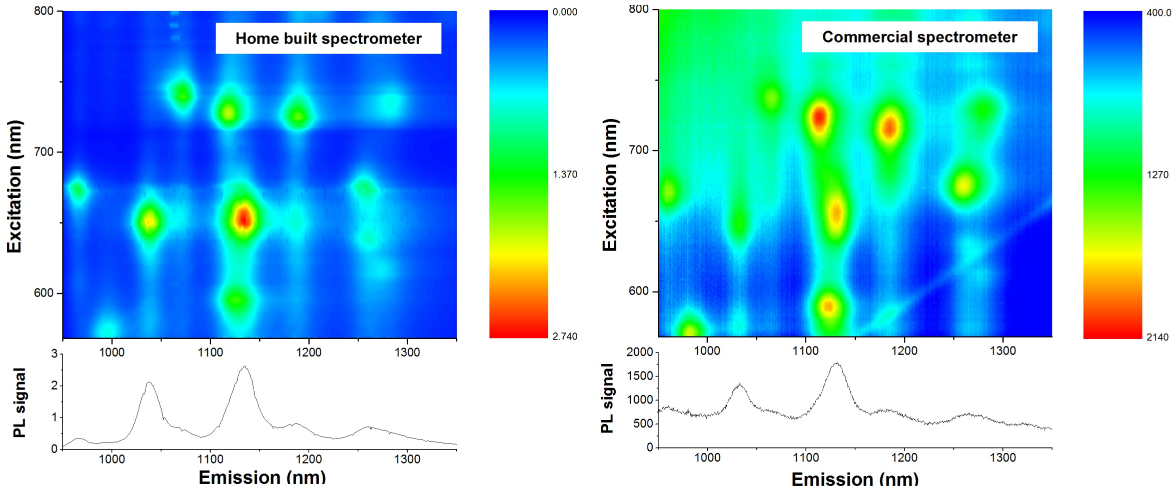

Figure 21: Comparison of a home-built spectrometer with the Fluorolog spectrometer from Horiba Jobin Yvon Ltd.: two PL map and the corresponding individual PL spectra are shown. Note the smaller contrast and a significant background for the measurement with the commercial spectrometer.

distribution, where the expected value and the variance are equal. In this case, the expected value is the signal and the variance is the noise. From that, we know that the number of pixels improves the signal-to-noise ratio by $\sqrt{1024} = 32$ for a given integration time.

Another difference between the two spectrometers is the collection optics: the commercial spectrometer has an $f/\# = 4.1$ and the home-built one has $f/\# = 1.2$. The number of collected photons goes with the square of the f-number.

These two properties cause a factor 30 higher sensitivity of our spectrometer. In Figure 21 this difference is shown, where a factor 40 times larger signal-to-noise ratio was observed for the same measurement time. Other advantages of the home-built spectrometer to mention are the use of more efficient filters and the absence of the baseline.

A disadvantage of our instrument that change of the laser excitation wavelength is not automatized.

3.2 ODMR spectroscopy

First of all, we perform a magnetic field sweep while the grating of the spectrograph is adjusted to a given wavelength in order to find the magnetic resonance of the nanotubes.

We chose an excitation and emission wavelength where a PL peak of an SWCNT is observable. In the meantime, ODMR signal is detected with the lock-in amplifier as a function of the magnetic field. The result of a magnetic field sweep is shown in Figure 22. Here, the wavelength of the excitation is $\lambda_{exc} = 1086\,\mathrm{nm}$ and we measure the emitted light at $\lambda_{em} = 730\,\mathrm{nm}$ wavelength.

The next step is that we fix the magnetic field to the maximum then perform a wavelength resolved ODMR study: we measure the change of the PL signal with the lock-in amplifier. In Figure 23 the simultaneously detected PL and ODMR spectra are shown for 730 nm excitation.

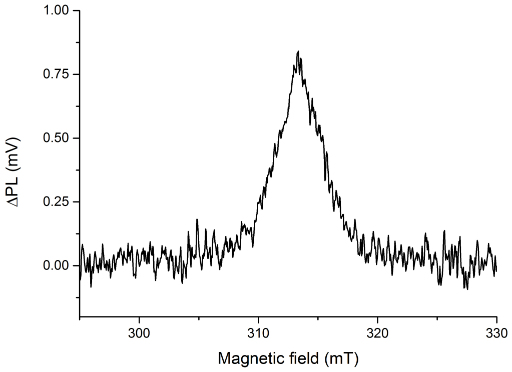

Figure 22: *Magnetic field swept ODMR signal.*

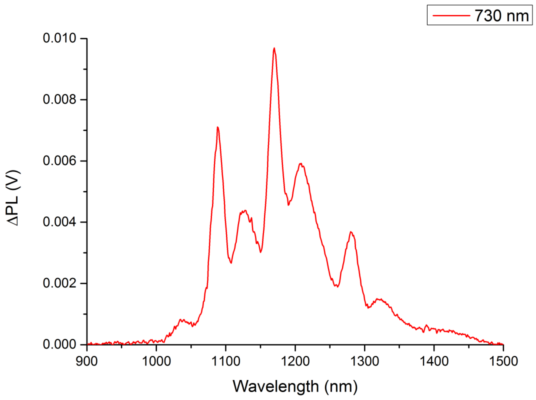

Figure 23: *The ΔPL (or ODMR) signal of SWCNTs.*

3.2.1 The spectrometer setup

The basic apparatus for ODMR measurements is the following: excitation light source, light collection optics and detector, microwave oscillator, magnet and cryostat. The commonly used method is to continuously chop the microwave irradiation and to detect the change in the collected light in-phase with the chopping using a lock-in amplifier since a small signal has to be isolated from a large background.

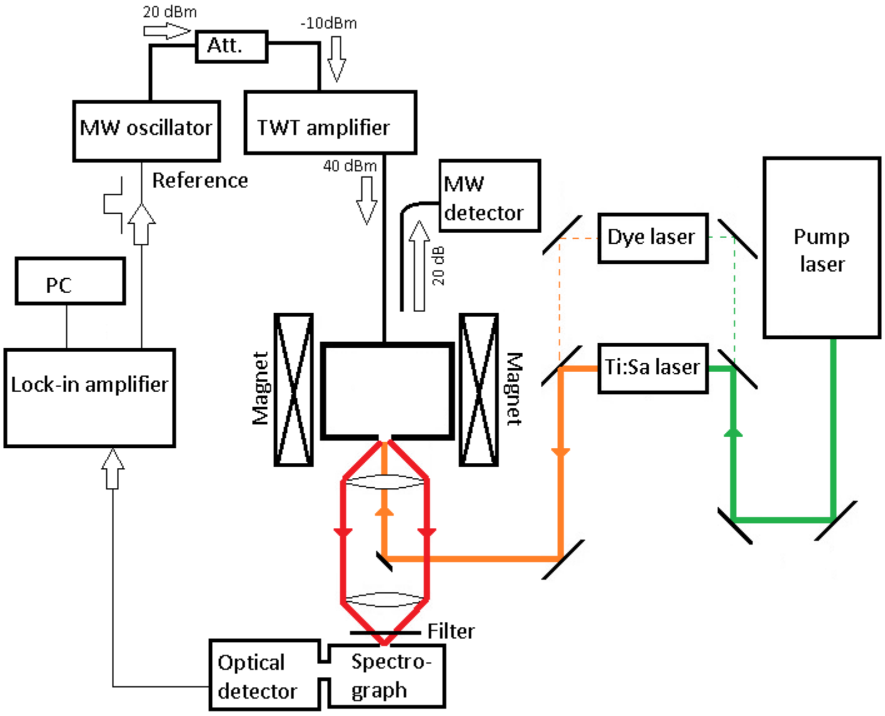

Figure 24: The experimental setup of the ODMR measurements on SWCNTs.[20]

The layout of the ODMR measurements is shown in Figure 24. The optical setup is the same as the one detailed above about the photoluminescence spectroscopy. One difference is that in this case the detector current is converted to voltage and measured with a lock-in amplifier.

The first element of the magnetic resonance setup is the microwave oscillator, which is a *HP83751B* microwave signal generator (output: 2-20 GHz). For the best signal-to-noise ratio, this source is used at maximum output power thus amplitude noise is decreased. The signal is chopped by a square wave from the lock-in amplifier around 1 kHz frequency.

After a passive attenuator (-10 dBM), the signal passes into a traveling wave tube (TWT) amplifier (*Varian WZX6980G2*) which provides a microwave output power of 40 dBm. This microwave signal is fed into a critically coupled microwave cavity, i.e. no power is reflected back towards the source, which lies between the magnets. For easy adjustment, a small amount of the reflected power (about 1%) is lead to a microwave detector (*HP8742B*) to measure it. Because the frequency is not constant, we need to apply an automatic frequency control (AFC) method to lock the frequency, for which the reflected signal is used.

The DC magnetic field is provided by an electromagnet stabilized by a Hall-probe and a feedback system.

3.2.2 Noise of the measurement

For measuring ODMR, we need to detect a small change in the fluorescence signal. The typical ODMR/PL ratio is $10^{-5}..10^{-6}$ therefore it is crucial to reduce the noise below this value. Another important fact to consider before the measurements that the sensitivity of detectors depends on the frequency. In our case, the detector has a band-width in the 100 Hz-1 kHz range with a 6 dB point at 2200 Hz due to the low frequency pass detector filtering. This limits the microwave chopping frequency.

The noise sources are the following in our system: oscillator noise of the laser, mechanical instabilities, detector noise and shot noise. The mechanical instabilities can be reduced below the others.

The detector noise and shot noise have white frequency characteristics, however, the noise of the laser is strongly frequency dependent (here frequency means the lock-in frequency). The oscillator noise is caused by the spontaneous emission which competes with the stimulated emission in the oscillator. To characterize this value, relative intensity noise (RIN) is measured, which describes the noise power per unit frequency bandwidth relative to the output power at a specified frequency separation from the carrier.

$$RIN = log_{10}\Big(\frac{\delta P}{P_c}\Big) \tag{24}$$

Here, δP is the noise and P_c is the DC power of the laser. RIN is measured in the 1-1000 Hz range using a fast photodiode connected to a lock-in amplifier. We note that RIN follows roughly RIN(f) $= -30 - 8 \cdot log_{10}(f)$ [dBc/$\sqrt{\text{Hz}}$] and it reaches RIN=-54 [dBc/$\sqrt{\text{Hz}}$] at 1 kHz. This means that our spectrometer can measure ODMR signal with $\Delta PL/PL = 4 \cdot 10^{-6}$ for a time constant of 1 second for 1 kHz microwave chopping frequency. This 1 kHz value is the optimal for ODMR spectroscopy with our NIR detector.

Because the shot noise depends on the power of the detected light, we need to analyze this aspect of the measurement for minimizing the noises. The intensity dependence of the signal-to-noise ratio (SNR) for shot noise:

$$SNR \sim \sqrt{I_{\text{incoming}}} \sim \sqrt{N_{\text{photon}}} \tag{25}$$

The sensitivity of the detector is described by the noise-equivalent power (NEP), the signal power that gives a signal-to-noise ratio of one in a one hertz output bandwidth. In our system, this value is $10^{-14}\,\mathrm{W}/\sqrt{\mathrm{Hz}}$ which corresponds to $N_{\text{NEP}} = 6 \cdot 10^4$ photons per seconds where one photon has 1 eV energy. The saturation of the detector occurs for an incoming power of $10^{-9}\,\mathrm{W}$ corresponding to $N_{\text{saturation}} = 6 \cdot 10^9$ photon flux. The detector noise is directly proportional to the incoming intensity and the number of photons. It means that the shot noise is 25% larger than the detector noise for the saturation and the incoming power is optimal if it is close to the saturation of the detector. This corresponds to about 200 mW power.

4 Results and discussion

4.1 Sample preparation

Investigation of carbon nanotubes happens in the form of suspension. During the preparation, sodium-deoxycholate (DOC) surfactant is mixed with distilled water in ultrasonic bath making a 2 % solution, then single-walled carbon nanotube samples are mingled with the solution.

The nanotubes used for the measurements are made by high-pressure CO conversion (*Carbon Nanotechnologies Inc.*) which is a type of the chemical vapor deposition techniques. High pressure and preheated CO and a catalyst precursor gas are mixed, then the gas decomposes and forms metal particle clusters on which carbon nanotubes nucleate and grow.

The mixture is sonicated with a tip-sonicator (*Bransor Sonifier 450*) for an hour with 60% output intensity. During the sonication, the suspension is cooled with a circulating water system. This process makes the nanotubes individualized since the surfactant molecules envelops the nanotube and prevent the formation of bundles. It can also happen that the individualization is not perfect and the sonication makes only smaller bundles.

The next step is to ultracentrifugate (*Elma Transsonic TI-H-10*) the samples with 200 kg for an hour. During this part of the preparation, the nanotubes with larger mass settle down at the bottom of the cuvette. This is necessary to remove the larger bundles left after sonication. Finally, the sample is decanted from the top of the suspension and placed into a 4 mm diameter quartz tube (Figure 25).

The measurements are carried out with the sample described above. However, another task was to reproduce the sample and improve the preparation making samples with stronger PL signal. To achieve the possible greatest signal, we varied the parameters of the preparation systematically and made control measurements to follow the changes. In Figure 26, a few data from optical absorption measurements are shown about the potential samples.

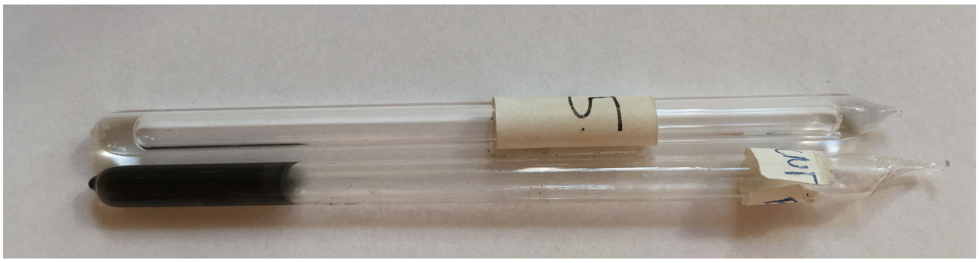

Figure 25: *SWCNT samples in quartz tubes. The black sample is made according to the above recipe, whereas the transparent sample is a previous preparation, without optimization.*

The conclusions of the sample preparation are the following:

- The suspension with more nanotubes generally gives a better signal. However, when using too much material, its majority will not mix well with the suspension and it settles down on the bottom of the cuvette.

- The longer sonication time increases the strength of the PL signal, but after 4 hours there is no significant improvement.
- The acceleration of ultracentrifuge has to be high in order to obtain a final sample with the majority of single nanotubes. However, the modification of this value has no effect on the signal above 200 kg.
- The recipe of the best sample: 0.010 g nanotubes in 2 % DOC solution, sonicating for 5 hours then ultracentrifuging at 500 kg for half an hour.

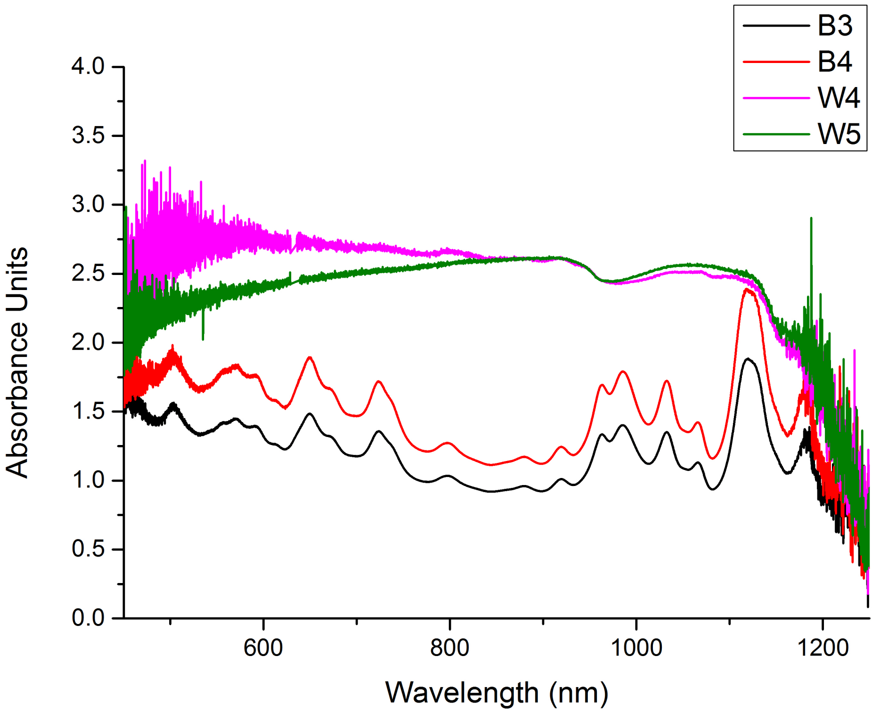

Figure 26: *Optical absorption measurements on SWCNTs. On the spectrum of the B4 and B3 samples, we observe narrow peaks which correspond to a given nanotube such as in case of the photoluminescence spectroscopy. Note that these peaks are absent in the W4 and W5 samples. It shows that these samples do not have PL signal.*

4.2 Evaluation of the data

The ODMR and PL spectra were measured by changing the excitation light in 6 nm steps by rotating the Lyot-filter in the laser using a microscrew. The intensity of the laser light also changed, so the raw data were first normalized to 100 mW, then we subtracted a constant baseline from them. Finally, all the data were interlaced in order to create a map. To achieve this, we used an evaluation program written in MATLAB.

Motivation for writing this script is to reduce the time of evaluation, because it is optimal if the time taken to process the data does not exceed the measurements or it is negligible.

The data series were saved that their names include important data such as the excitation wavelength and the power of the excitation light. The program looks for these information, collects the wavelength into a matrix, and normalize the intensities with the power. From the wavelength, the energy of the optical transitions in eV is calculated, which will be important later.

To erase the baseline, the average of the last 50 data is subtracted from the intensity values for every spectrum. Our detector is not sensitive in this domain and these data show only the noise. After the corrections, the intensities are sorted into a matrix. Finally, it presents the measurement data in several ways.

The code is found in Appendix A.

4.3 Analysis

4.3.1 ODMR on single-walled carbon nanotubes

Figure 27 compares the results of the simultaneously taken PL and ODMR measurements for a given excitation. An interesting thing to consider that the two spectra appear to be dissimilar: the intensities of the peaks have a different ratio. It caused by the fact that the change of the PL signal, i.e. the ODMR signal, only depends on the populations and decay rates of the triplet sublevels and is independent on the strength of the original PL signal. The dynamics of the triplet states are different for every nanotube.

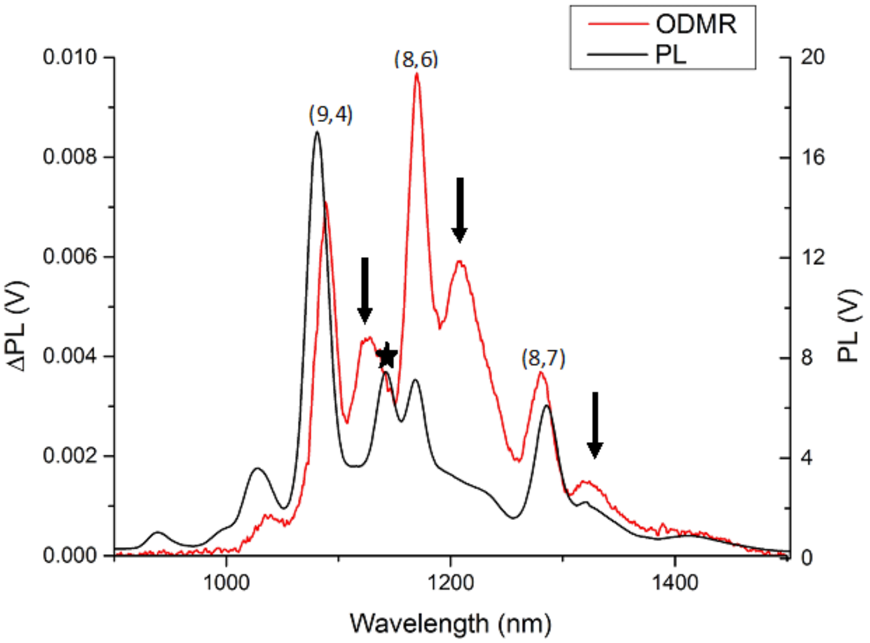

Figure 27: *Simultaneously measured ODMR and PL spectrum for* 730 nm *excitation. Note that the ratio of the PL and ODMR signals is not constant in the spectra. The* (n, m) *indices show the chirality peaks. Arrows denote the phosphorescence peaks and star marks the so-called bundle peak.*

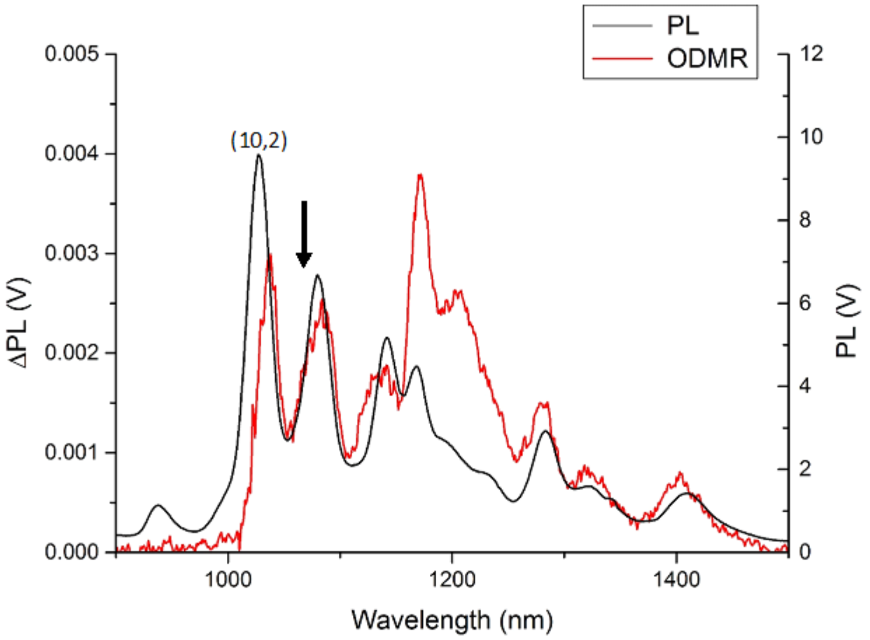

Figure 28: *Simultanously measured ODMR and PL spectrum for* 748 nm *excitation. The phosphorescence sideband is marked by arrow.*

Another detail to note is that new peaks appear on the ODMR spectrum which are absent from the PL measurements. These peaks belong to the phosphorence signals. They are not present on the PL spectrum, because the fluorescence path is the dominant for the ligth radiation. In turn, under microwaves irradiation, we change not only the intensity of the fluoresence, but the strength of the phosphoresence signal, as well. Given that we use a lock-in detection, the corresponding phosphorescence signal is clearly observed. There is another difference: a peak denoted by star is absent on the ODMR spectrum. This additional peak does not belong to any nanotube. It is a so-called bundle peak, whose excitation wavelength is determined by a given nanotube and its emission wavelength belongs to another one. This interesting phenomenon is discussed below in detail. Figure 28 shows another comparison of the ODMR and PL spectra at 748 nm, where the $(10, 2)$ nanotube has a maximum. Its phosphoresence sideband fades into the fluorescence peak of another nanotube.

In Figures 29-32, ODMR and PL spectra are shown, however, in this case the data are presented as a function of excitation wavelength. We find that the chirality peaks, which belong to different nanotubes, are detected at the same wavelength whereas their intensities are different. As consequence of this observation is that we indeed detect the change of the fluorescence signal during the ODMR measurement.

In Figure 33, a so-called ODMR map is presented, which is made by combining the ODMR spectra following the process discussed above in Section 4.3. In order to follow the change of the peak positions, a similar PL map is also created and is shown in this figure. The emission spectra are taken with excitation from 712 nm to 820 nm in 6 nm steps.

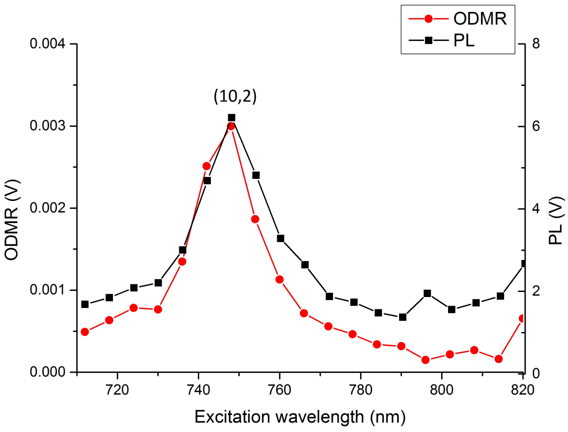

Figure 29: *Emission:* 1038 *nm*

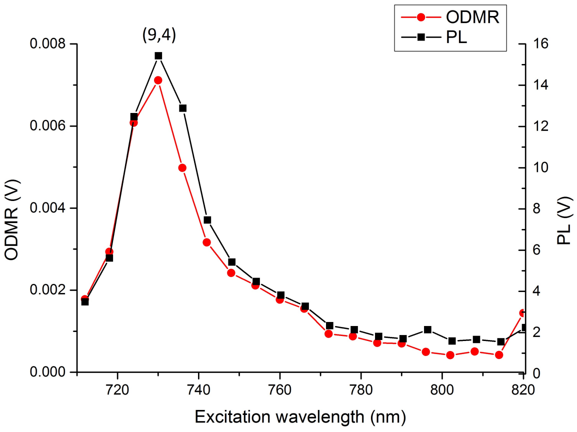

Figure 30: *Emission:* 1088 *nm*

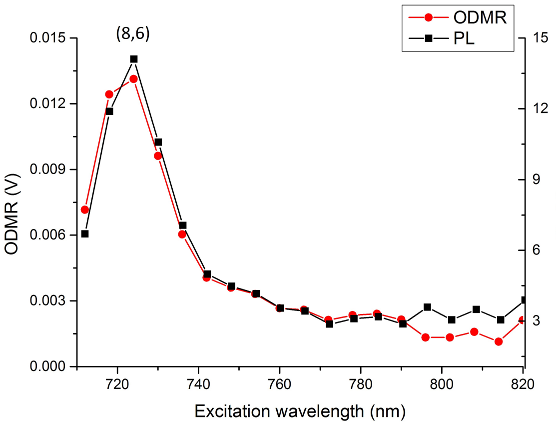

Figure 31: *Emission:* 1169 *nm*

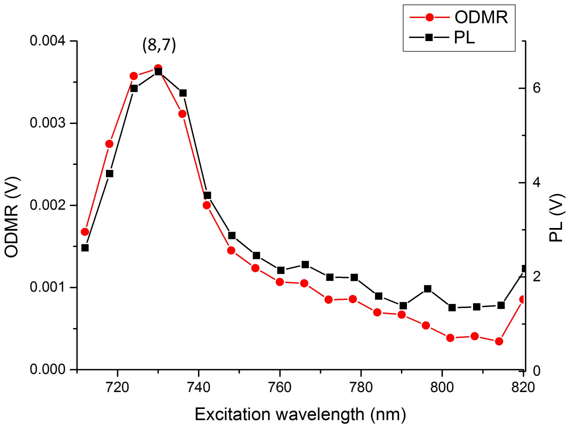

Figure 32: *Emission:* 1281 *nm*

On the PL map, the spots of the nanotubes are denoted by crosses. These data, the (n, m) pairs and the belonging excitation and emission wavelength, are presented in the work of Weisman and Bachilo [5]. Note that there is a difference between the literature data and the actual chirality peaks, which is caused by the temperature difference and a different surfactant used. The calculated data show the PL peak positions at 300 K and our measurements are taken at 77 K. In Ref. [5], sodium-dodecyl-sulphate (SDS) was used as a surfactant.

The figure shows distinct peaks with variable signal strength. However, it is noted that not all (n, m) pairs can be assigned to a chirality peak. First of all, we know that zig-zag nanotubes $(m = 0)$ do not have a photoluminescence signal. The explanation of this effect is currently unknown [18]. On the other hand, the distribution of the diameters follows a Gaussian function, therefore nanotubes with larger diameter are not present in the sample.

The carbon nanotubes for which the $2n + m$ equation give the same value is classified into a so-called family [17]. These nanotubes have similar optical behavior and as shown in Figure 33, the peaks belonging to one family are located on so-called branches close to each other. Another observation on the PL map is the presence of the above discussed vertical lines which are caused by the vibrational relaxation or internal conversion.

The arrows indicate at the phosphorescence peaks. Note that the phosphorescence sidebands appear not only on the ODMR map but they are present on the PL map, as well. The intensities of these peaks are not significant compared to the fluorescence signals. Star denotes a bundle peak.

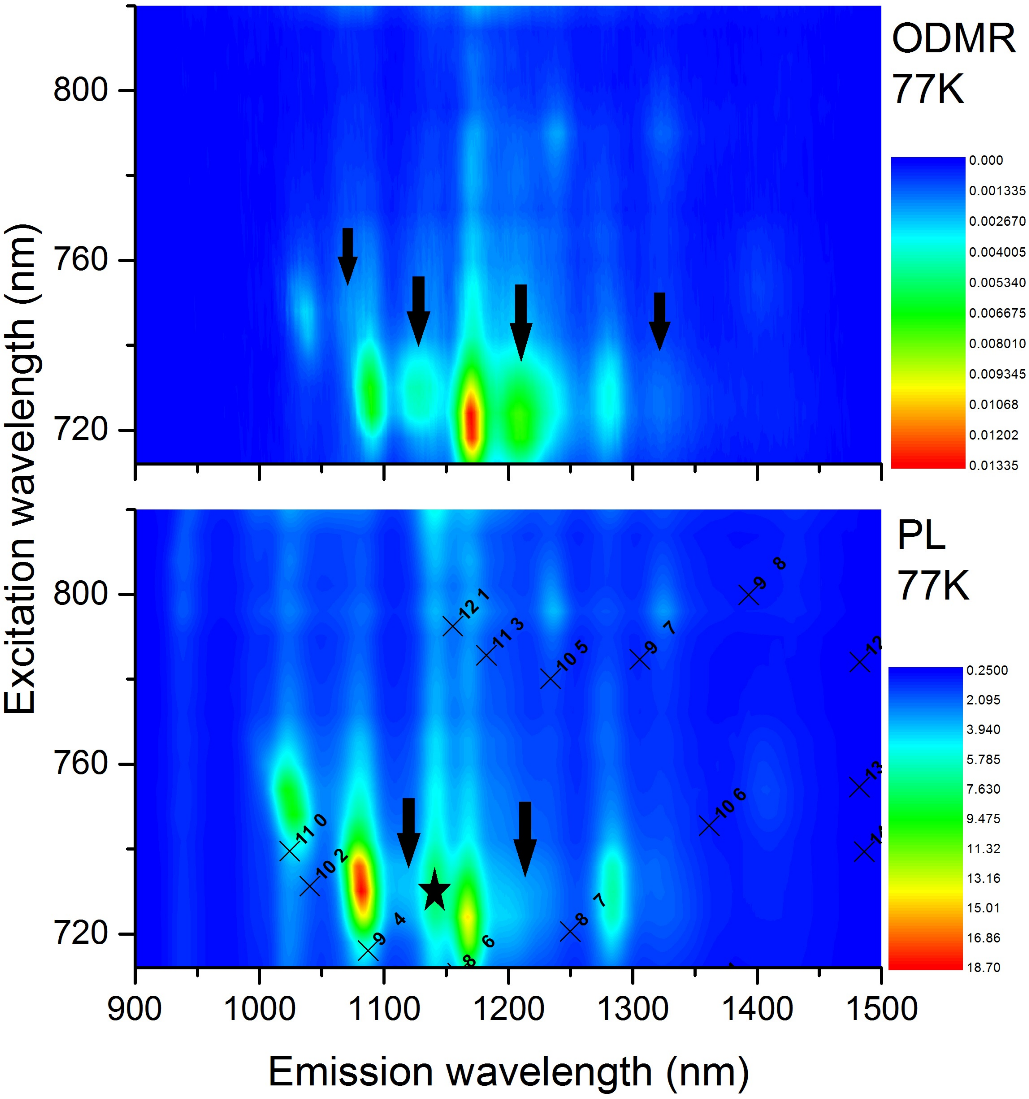

Figure 33: *2D representation of the measured data: ODMR and PL map. The crosses mark the expected position of the chirality peaks and the arrows show the phosphorescence peaks. The* (n, m) *indices are also denoted from Ref. [5]. The star indicates the bundle peak.*

In Figures 34-37, the cross section of the ODMR map are shown at different emission wavelengths. We chose the wavelength where the strength of the fluorescence peak is the strongest and compare it with the excitation spectrum where the phosphorescence sideband of the peak is observable. We present this comparison for the largest chirality peaks and we can see that the phosphorescence peaks can be excited at the same wavelength than the fluorescence ones.

We measured the spectra in 6 nm steps, which limits the resolution of this type of data.

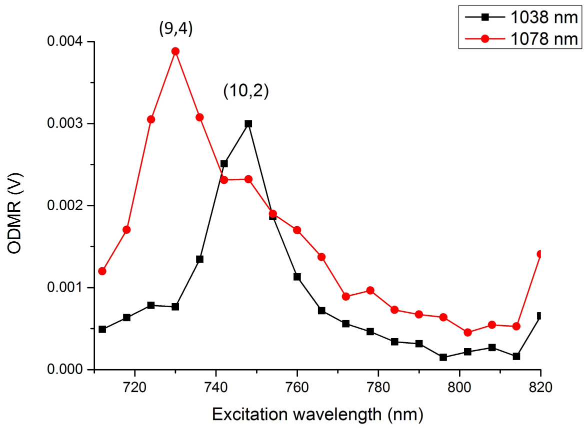

Figure 34: (10, 2) chirality peak has a maximum at 1038 nm emission wavelength. Its sideband is observable at 1078 nm.

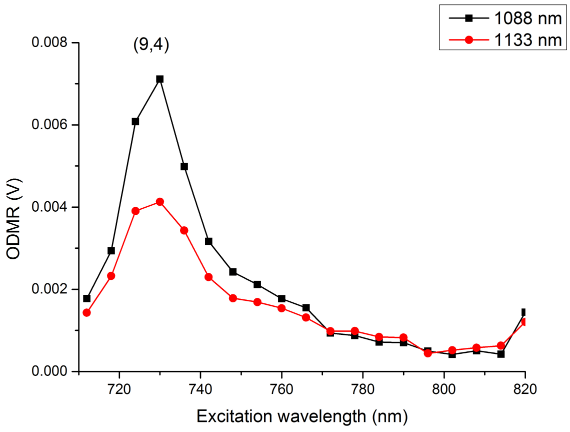

Figure 35: (9, 4) chirality peak has a maximum at 1088 nm emission wavelength. Its sideband is observable at 1133 nm.

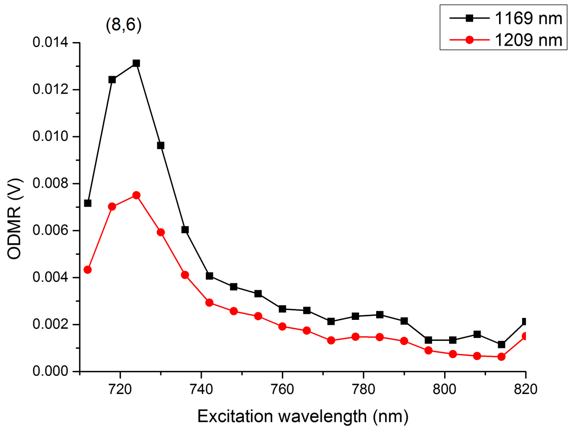

Figure 36: (8, 6) chirality peak has a maximum at 1169,nm emission wavelength. Its sideband is observable at 1209 nm.

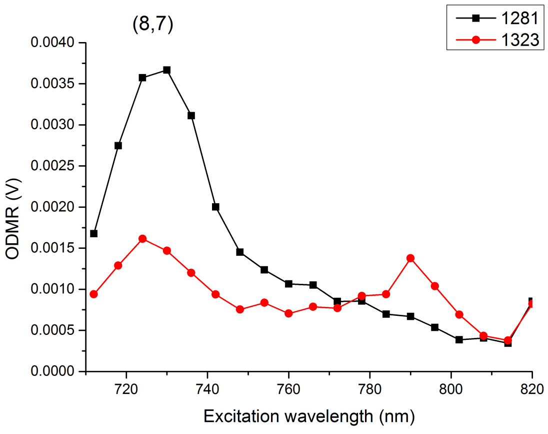

Figure 37: (8, 7) chirality peak has a maximum at 1281 nm emission wavelength. Its sideband is observable at 1323 nm.

4.3.2 Singlet-triplet gap

We can identify the different peaks on the ODMR maps as belonging to the different SWCNT chiralities. Positions of the fluorescence peaks and the phosphorescence sidebands are determined from Figure 33.

In Table 1, data of the larger peaks are collected such as the (n, m) indices and the family which they belong to. The calculated value of the emission (λ_{em}) and excitation wavelength (λ_{exc}) expected at room temperature from the literature data are also listed.

(n,m)	Family 2n+m	Literature value λ_{exc} (nm)	Literature value λ_{em} (nm)	F λ_{exc} (nm)	F λ_{em} (nm)	Ph λ_{exc} (nm)	Ph λ_{em} (nm)
(10,2)	22	731	1041	748	1038	748	1078
(9,4)	22	716	1087	730	1088	730	1130
(8,6)	22	711	1159	724	1169	724	1209
(8,7)	23	721	1250	727	1281	727	1323

Table 1: Positions of the fluorescence (F) and phosphorescence (Ph) peaks as determined from the ODMR map.

(n,m)	Diameter d (nm)	Excitation E_{22} (eV)	F E_{11} (eV)	Ph E_T (eV)	S-T gap ΔE_{ST} (meV)
(10,2)	0.87231	1.65842	1.19509	1.15074	44.35
(9,4)	0.90342	1.69932	1.14017	1.09973	40.44
(8,6)	0.953	1.7134	1.06026	1.02605	34.21
(8,7)	1.01837	1.70633	0.96914	0.9412	27.94

Table 2: Singlet-triplet gap of single-walled carbon nanotubes.

In Table 2, the same nanotubes are collected with their diameters calculated from equation 2. In this case, the excitation energies, which correspond to the second optical transitions and the emission energies of the fluorescence and phosphorescence peaks are presented in eV according to the following conversion formula:.

$$E = \frac{\hbar \cdot \pi}{\lambda} \cdot c \approx 1240.5 \cdot \frac{1}{\lambda} [eV] \tag{26}$$

In the last column, the difference of these two peaks is shown which is equal to the gap of the singlet and triplet energy levels. Since the emission energy of the fluorescence peak is the energy difference of the S_0 and S_1 singlet states i.e. the 1^{st} optical transition (E_{11}) and the phosphorescence peak is the energy difference of the S_0 singlet ground state and T triplet state.

According to the nearest-neighbor tight-binding approximation, the optical transition energy of the semiconducting nanotubes depends on their geometry following equation 7. In Figure 38 the energy difference is shown as a function of the diameter. We found a purely empirical relation for the singlet triplet energy gap: $E(d) = \frac{100.52}{d} - 70.94\,[\text{meV}]$.

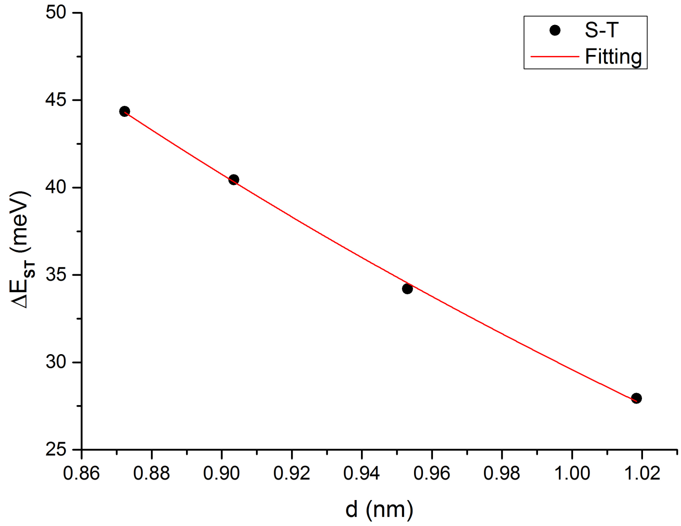

Figure 38: *The energy difference of the S_1 and T states as a function of the diameter of nanotubes. Solid line shows a fit as explained in the text.*

It is beyond the scope of the present work to explain this relation. We only motivate the $1/d$ diameter dependence. It is probably due to a confinement effect: the spin-triplet state corresponds to an anti-symmetric wavefunction in real space which has a lower Coulomb energy. This energy gain is larger if the nanotube is smaller, i.e. the exciton wavefunction is more localized.

4.3.3 Bundle peaks on the PL map

Carbon nanotubes are arranged in bundles in a real sample and because it is difficult to isolate them completely, another process is observable during the measurements. In bundles, nanotubes are close enough that exciting one with a given energy, it can transfer its energy to another nanotube and the emission can be generated here [15]. This is shown in Figure 39.

As a result of that, peaks appear on the PL map, which cannot be associated with any (n, m) chiralities. These, so-called bundle peaks lie in the intersection of the excitation energy for one nanotube and the emission energy of another. Based on this, the bundle peaks present on the PL map where the emission wavelength of a nanotube intersects the excitation wavelength of another one. The existence of the bundle peaks is a direct consequence of the E_{22} and E_{11} irregularities as compared to the simples $1/d$ rule in nanotubes: it is common that E_{22} for an SWCNT becomes larger than the $1/d$ rule would dictate, whereas the E_{11} becomes smaller [5].

In Table 3, the emission and excitation wavelength and energies of a bundle peak marked by **B** are presented. The table also shows the nanotubes which take part in the creation of the peak. The data are read from the PL map (Figure 33).

This additional peak appears only on the PL map and is completely absent on the ODMR map. Further considerations are required to explain this observation.

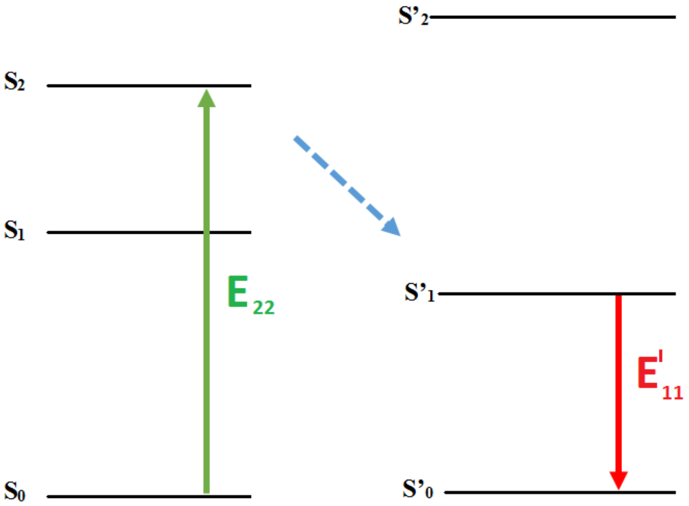

Figure 39: *Schematic representation of a bundle PL related process. A nanotube gives away its energy to another nanotube. The excitation (E_{22}) occurs on the first nanotube, however, in turn the photon is emitted (E'_{11}) by the second one.*

	(n,m)		λ_{exc} (nm)	λ_{em} (nm)	E_{22} (eV)	E'_{11} (eV)
B	$(9,4)$	$(7,6)$	730	114	1.699	1.086

Table 3

The scheme of this process is depicted in Figure 40, when an exciton jumps to another nanotube in a bundle, it emits a photon with E'_{11} energy, or it is transferred to the triplet state and does phosphorescence radiation with k'_T decay rate. Regardless of which process occurs, the nanotube reaches the S'_0 ground state and the nanotube, from which the exciton originates, also reaches the S_0 ground state upon transfering the exciton.

For a one-nanotube ODMR process the ODMR signal is a consequence of the triplet population change due to the microwave irradiation. For the bundle peak in principle both the T and T' states can be populated, i.e. a strong ODMR signal would be expected. The first observation is that the bundle peak intensity itself is unaffected by the T' state population as the S'_1 population only depends on the exciton transfer process (that process "pumps" the S'_1 population). In principle a phosporescent peak near the bundle peak would be observable but it overlaps with other signal we are therefore unable to resolve it.

The remaining question is why the T population does not affect the bundle peak. In our opinion, the only possible explanation of the experimental result is that the T state is not populated at all for the bundle PL process. It means that the exciton transfer to the neighboring tube in a bundle is preferred as compared to an internal conversion process, either from the S_2 or from the S_1 (strong arrows in Figure 40)

Following the above qualitative considerations, we give a more quantitative discussion. We can investigate the population dynamics of the two nanotubes. First of all, we can determine the number of the excitable electrons.

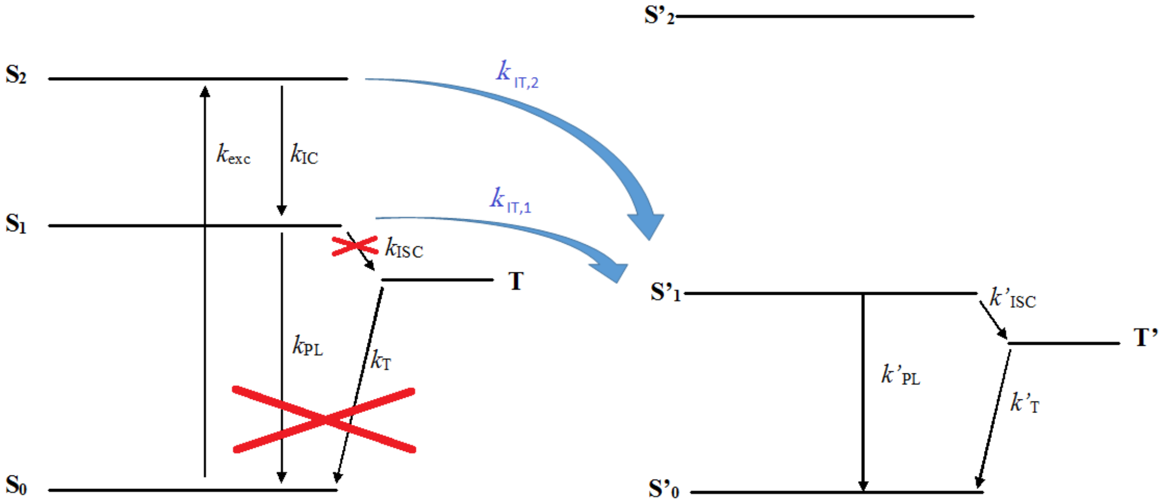

Figure 40: *Photoluminescence process leading to a bundle peak. The decay rates and photon emitting probabilities are presented. Note that the excitation can only occur on the first nanotube. The exciton always jumps to the second nanotube, therefore the fluorescence* (k_{PL}) *and phosphorescence* (k_T) *processes are not measured.*

$$N = [S_0] + [S_1] + [S_2] + [S_0'] + [S_1'] + \sum_{u=0}^{3} [T_{\text{u}}'] \approx [S_0] + [S_0'] + \sum_{u=0}^{3} [T_{\text{u}}'] \tag{27}$$

Here, we take into account that $[S_1]$, $[S_2]$ and $[S_1']$ are negligible since the lifetime of these states are shorter.

Because in bundles, the exciton always jumps to the acceptor nanotube, the population of the ground state of the donor nanotube only depends on the k_{exc} excitation probability and is not affected by the decay rates of the excited states.

$$\frac{\mathrm{d}[S_0]}{\mathrm{d}t} = -k_{\text{exc}}[S_0] \tag{28}$$

The transition between the tubes are described by $k_{\text{IT},1}$ and $k_{\text{IT},2}$, because from these data we cannot decide from which excited state the transition occurs: S_1 or S_2. We assume that the two processes, the internal conversion and the jump between the nanotubes, compete with each other on the S_2 excited state.

$$\frac{\mathrm{d}[S_1]}{\mathrm{d}t} = k_{\text{IC}}[S_2] - k_{\text{IT},1}[S_1] \tag{29}$$

$$\frac{\mathrm{d}[S_2]}{\mathrm{d}t} = k_{\text{exc}}[S_0] - k_{\text{IC}}[S_2] - k_{\text{IT},2}[S_2] \tag{30}$$

For the following differential equations, we assume that excitons on the second nanotube drop out from the photoluminescence cycle and they can only get to the acceptor tube from the donor tube.

$$\frac{\mathrm{d}[S_0']}{\mathrm{d}t} = k_{\mathrm{PL}}'[S_1'] + \sum_{u=0}^{3} k_{\mathrm{u}}'[T_{\mathrm{u}}'] \tag{31}$$

$$\frac{\mathrm{d}[T_{\mathrm{u}}']}{\mathrm{d}t} = k_{\mathrm{ISC}}' P_{\mathrm{u}}[S_1'] - k_{\mathrm{u}}'[T_{\mathrm{u}}'] \tag{32}$$

$$\begin{aligned} \frac{\mathrm{d}[S_1']}{\mathrm{d}t} &= k_{\mathrm{IT},2}[S_2] + k_{\mathrm{IT},1}[S_1] - \sum_{u=0}^{3} k_{\mathrm{ISC}}' P_{\mathrm{u}}'[S_1'] - k_{\mathrm{PL}}'[S_1'] = \\ &= k_{\mathrm{IT},2}[S_2] + k_{\mathrm{IT},1}[S_1] - (k_{\mathrm{ISC}}' + k_{\mathrm{PL}}')[S_1'] \end{aligned} \tag{33}$$

The intensity of the bundle peak depends on the population of the S_1' state, where the fluoresence radiation occurs from. It is clear that $[S_1']$ is not affected by k_u' decay rates and the change of the population of the triplet sublevels, which occurs under continous microwave irradiation. These considerations thus explain why the bundle peak is absent on the ODMR map.

5 Summary

In this thesis, I reviewed the most important optical properties and the details of the energy structure of the single-walled carbon nanotubes, which have a potential applications in light harvesting and generation. I discussed the application of the optically detected magnetic resonance method, which is suitable for investigating the energy structure of these nanomaterials.

I presented the samples used for the measurements and their preparation process. I described a recipe to reproduce them and improve the preparation. I automated the evaluation of measured data, significantly accelerating this process that would be lengthy on all spectra.

To characterize the chirality peaks of the nanotubes on the ODMR map, I analyzed the previously measured data. From the emission energy of the chirality peaks, I determined the chirality dependent singlet-triplet gaps of the nanotubes and found an empirical relation depending on the geometry of the nanotubes.

In this thesis, a new phenomenon is also interpreted, the behavior of bundle peaks on the ODMR map.

Appendix

A MATLAB script

The program written in MATLAB for the evaluation of the measurement.

First, it opens a txt document that contains the names of the data to be read, then a cycle run through the listed names.

```
id =fopen('filename.txt');
i=0;

while feof(id) == 0
    i = i+1;
    FileName = fscanf(id,'%s',1);
```

In the name of the document, the power of the laser light and the excitation wavelength is denoted that the program read out here.

```
    p = regexp(FileName, '\ d{1,3}m[wW]', 'match');
    p=p {1};
    p=str2num(p(1:end-2));

    w = regexp(FileName, '\ d{1,3}nm', 'match');
    w=w{1};
    w=str2num(w(1:end-2));
```

The excitation wavelength are listed to a column vector. The excitation energy can be calculated from this.

```
    WaveLength(i,1)=w;
    ExcEnergy(i)=1240.5/WaveLength(i);

    Temp = importdata(FileName,',',6);
```

After reading the data, they are normalized by power then organized in matrices. Here, we can give that at which wavelength (lambda) we want to correct the data and how (k).

```
    lambda=600;
    k=1;
    if    w=lambda
            Intensity(:,i)=(100/p)*Temp(:,2)*k;
    else
            Intensity(:,i)=(100/p)*Temp(:,2);
```

```
    end;
end;

fclose(id);

[s,o]=size(Intensity);

for i=1:s
    EmEnergy(i,1)=1240.5/Temp(i,1);
end;
```

Subtraction of the baseline.

```
for i=1:o
    alap=0;
    for    k=650:700
           alap=alap+Intensity(k,i);
    end;
    alap=alap/51;
    for j=1:s
           Intensity(j,i)=Intensity(j,i)-alap;
    end;
end;
```

Map_xyz: Ordering the data to the map. The first column is the emitted wavelength, the second is the excitation wavelength, and the third is the normalized data without the basline.

```
n=1;
for i=1:o
    m=n+(s-1);
    Map_xyz(n:m,2)=WaveLength(i);
    Map_xyz(n:m,1)=Temp(:,1);
    Map_xyz(n:m,3)=Intensity(:,i)*1;
    n=n+s;
end;
```

Map_exc: Ordering the matrix that the data with the same excitation wavelength are in one column.

Map_em: Transposed of the previous one.

```
for i=1:o
    Map_exc(:,i)=Intensity(:,i);
end
```

```
    Map_em=Map_exc’;

save(’Map_exc.txt’, ’Map_exc’, ’-ascii’)
save(’Map_em.txt’, ’Map_em’, ’-ascii’)
```

The data are chosen that only every j^{th} is read.

```
j=6;
m=floor(s/j);

k=1;
for i=1:m
    Map_exc2(i,:)=Map_exc(k,:);
    k=k+6;
end;

[x,y]=size(Map_xyz);
x=floor(x/6);
k=1;
for i=1:x
    Map_xyz2(i,:)=Map_xyz(k,:);
    k=k+6;
end;
```

We can also order the data to the map calculating the energy from the excitation and emitted wavelengths first.

```
n=1;
for i=1:o
    m=n+(s-1);
    Map_xyz_eV(n:m,2)=ExcEnergy(i);
    Map_xyz_eV(n:m,1)=EmEnergy(:,1);
    Map_xyz_eV(n:m,3)=Intensity(:,i);
    n=n+s;
    end;
```

The data are chosen that only every j^{th} is read.

```
[x,y]=size(Map_xyz_eV);
j=6;
x=floor(x/j);
k=1;
for   i=1:x
    Map_xyz2_eV(i,:)=Map_xyz_eV(k,:);
```

```
    k=k+6;
end;
```

References

[1] Sumio Iijima. *Helical microtubules of graphitic carbon* Nature, 354:56–58, 1991

[2] S. Iijima, T. Ichihashi. *Single-shell carbon nanotubes of 1-nm diameter* Nature, 363:603-605, 1993

[3] Bethune et al.*Cobalt-catalysed growth of carbon nanotubes with single-atomic-layer walls* Nature, 363:605-607, 1993

[4] N. Hamada, S. Sawada and A. Oshiyama. *New one-dimensional conductors: Graphitic microtubules.* Physical Review Letters, 68:1579.1581, 1992.

[5] Sergei M. Bachilo, Michael S. Strano, Carter Kittrell, Robert H.Hauge, Richard E. Smalley, and R. Bruce Weisman *Structure-Assigned Optical Spectra of Single-Walled Carbon Nanotubes* Science 20 December 2002: 298 (5602), 2361-2366. Published online 29. November 2002.

[6] M. S. Dresselhaus, G. Dresselhaus, and P. Avouris *Carbon Nanotubes: Synthesis, Structure, Properties, and Applications.* Springer, Berlin, Heidelberg, New York, 2001.

[7] R. Saito, G. Dresselhaus and M. S. Dresselhaus. *Physical Properties of Carbon Nanotubes.* Imperial College Press, 1998.

[8] X. Wei, T. Tanaka, N. Akizuki, Y. Miyauchi, K. Matsuda, M. Ohfuchi, and H. Kataura *Single-Chirality Separation and Optical Properties of (5,4) Single-Wall Carbon Nanotubes* J. Phys. Chem. C, 2016, 120 (19), pp 10705–10710

[9] A. Thess, R. Lee, P. Nikolaev, H. Dai, P. Petit, J. Robert, C. Xu, Y. H. Lee, S. G. Kim, A. G. Rinzler, D. T. Colbert, G. E. Scuseria, D. Tomanek, J. E. Fischer, R. E. Smalley *Crystalline Ropes of Metallic Carbon Nanotubes.* Science, 273:483-487, 1996.

[10] A. Loiseau, P. Launois, P. Petit, S. Roche, and J.-P. Salvetat. *Understanding Carbon Nanotubes: From Basics To Applications* volume 677 of Lecture Notes in Physics. Springer, 2006.

[11] H. Kataura, Y. Kumazawa, Y. Maniwa, I. Umezu, S. Suzuki, Y. Ohtsuka and Y. Achiba. *Optical properties of single-wall carbon nanotubes.* Synthetic Met., 103:2555–2558, 1999.

[12] S. G. Chou, F. Plentz, J. Jiang, R. Saito, D. Nezich, H. B. Ribeiro, A. Jorio, M. A. Pimenta, Ge. G. Samsonidze, A. P. Santos, M. Zheng, G. B. Onoa, E. D. Semke, G. Dresselhaus, and M. S. Dresselhaus. *Phonon-Assisted Excitonic Recombination Channels Observed in DNA-Wrapped Carbon Nanotubes Using Photoluminescence Spectroscopy* Physical Review Letters 94, 127402, 1. April 2005

[13] Péter Szirmai *Elektronspin-rezonancia alkáli atommal dópolt szén nanocsöveken, BSc Szakdolgozat* Budapest University of Technology and Economics, 2011

[14] A. Thess, R. Lee, P. Nikolaev, H. Dai, P. Petit, J. Robert, C. Xu, Y. H. Lee, S. G. Kim, A. G. Rinzler, D. T. Colbert, G. E. Scuseria, D. Tomanek, J. E. Fischer, R. E. Smalley *Crystalline Ropes of Metallic Carbon Nanotubes.* Science, 273:483-487, 1996

[15] Juan Yang , Nuoya Yang , Daqi Zhang , Xiao Wang , Yilun Li , and Yan Li. *Photoluminescence from Exciton Energy Transfer of Single-Walled Carbon Nanotube Bundles Dispersed in Ionic Liquids* J. Phys. Chem. C, 116 (41), pp 22028–22035, 2012

[16] Michael J. O'Connell, Sergei M. Bachilo, Chad B. Huffman, Valerie C. Moore, Michael S. Strano, Erik H. Haroz, Kristy L. Rialon, Peter J. Boul, William H. Noon, Carter Kittrell, Jianpeng Ma, Robert H. Hauge, R. Bruce Weisman, Richard E. Smalley. *Band Gap Fluorescence from Individual Single-Walled Carbon Nanotubes.* Science, Vol. 297 no. 5581 pp. 593-596, 26. July 2002

[17] Ge. G. Samsonidze, R. Saito, N. Kobayashi, A. Grüneis, J. Jiang, A. Jorio, S. G. Chou, G. Dresselhaus and M. S. Dresselhaus *Family behavior of the optical transition energies in single-wall carbon nanotubes of smaller diameters* Applied Physics Letters 85, 5703, 2004

[18] Stephanie Reich, Christian Thomsen, and John Robertson. *Exciton Resonances Quench the Photoluminescence of Zigzag Carbon Nanotubes* Physical Review Letters 95, 077402, 12. August 2005

[19] Feng Wang, Gordana Dukovic, Louis E. Brus, Tony F. Heinz *The Optical Resonances in Carbon Nanotubes Arise from Excitons* Science, Vol. 308 no. 5723 pp. 838-841, 6. May 2005

[20] Negyedi et al. *An optically detected magnetic resonance spectrometer with tunable laser excitation and wavelength resolved infrared detection* Review of Scientific Instruments 88, 013902, 2017

[21] Hannes Kraus *Optically Detected Magnetic Resonance on Organic and Inorganic Carbon-Based Semiconductors* University of Würzburg, 2014

[22] Donatella Carbonera *Optically detected magnetic resonance (ODMR) of photoexcited triplet states* Photosynth Res (2009) 102:403–414

[23] `http://www.ep4.phy.uni-bayreuth.de/ag_jkoehler/en/research/archive/odmr/index.html`, May 2017

[24] `http://www.univie.ac.at/spectroscopy/fks/forschung/ergebnisse/nanotubes.htm`, May 2017

[25] `http://www.photobiology.info/Visser-Rolinski.html`, May 2017

[26] `http://www.chemicool.com/definition/monochromators.html`, May 2017